Biomaterials 279 (2021) 121186

Contents lists available at ScienceDirect

Biomaterials

journal homepage: www.elsevier.com/locate/biomaterials

Nanostructured gold electrodes promote neural maturation and network connectivity

Ana Domínguez-Bajo [a,1], Juliana M. Rosa [b,1], Ankor González-Mayorga [b], Beatriz L. Rodilla [c,e], Ana Arché-Núñez [c], Esther Benayas [a], Pilar Ocón [d], Lucas Pérez [c,e], Julio Camarero [c,g], Rodolfo Miranda [c,g], M. Teresa González [c], Juan Aguilar [b,f], Elisa López-Dolado [b,f], María C. Serrano [a,*]

[a] Instituto de Ciencia de Materiales de Madrid (ICMM), CSIC, Calle Sor Juana Inés de la Cruz 3, 28049, Madrid, Spain
[b] Hospital Nacional de Parapléjicos, SESCAM, Finca La Peraleda s/n, 45071, Toledo, Spain
[c] Instituto Madrileño de Estudios Avanzados (IMDEA Nanociencia), Calle Faraday 9, 28049, Madrid, Spain
[d] Departamento de Química Física Aplicada, Universidad Autónoma de Madrid, 28049, Madrid, Spain
[e] Departamento de Física de Materiales, Universidad Complutense de Madrid, Plaza de las Ciencias s/n, 28040, Madrid, Spain
[f] Research Unit of "Design and development of biomaterials for neural regeneration", Hospital Nacional de Parapléjicos, Joint Research Unit with CSIC, Finca La Peraleda s/n, 45071, Toledo, Spain
[g] Instituto "Nicolás Cabrera" and Condensed Matter Physics Center (IFIMAC), Departamento de Física de la Materia Condensada, Universidad Autonoma de Madrid, Madrid, 28049, Spain

ARTICLE INFO

Keywords:
Gold
Live calcium dynamics
Nanostructured electrodes
Nanowires
Network connectivity
Spinal cord injury

ABSTRACT

Progress in the clinical application of recording and stimulation devices for neural diseases is still limited, mainly because of suboptimal material engineering and unfavorable interactions with biological entities. Nanotechnology is providing upgraded designs of materials to better mimic the native extracellular environment and attain more intimate contacts with individual neurons, besides allowing for the miniaturization of the electrodes. However, little progress has been done to date on the understanding of the biological impact that such neural interfaces have on neural network maturation and functionality. In this work, we elucidate the effect of a gold (Au) highly ordered nanostructure on the morphological and functional interactions with neural cells and tissues. Alumina-templated Au nanostructured electrodes composed of parallel nanowires of 160 nm in diameter and 1.2 μm in length (Au-NWs), with 320 nm of pitch, are designed and characterized. Equivalent non-structured Au electrodes (Au-Flat) are used for comparison. By using diverse techniques in *in vitro* cell cultures including live calcium imaging, we found that Au-NWs interfaced with primary neural cortical cells for up to 14 days allow neural networks growth and increase spontaneous activity and ability of neuronal synchronization, thus indicating that nanostructured features favor neuronal network. The enhancement in the number of glial cells found is hypothesized to be behind these beneficial functional effects. The *in vivo* effect of the implantation of these nanostructured electrodes and its potential relevance for future clinical applicability has been explored in an experimental model of rat spinal cord injury. Subacute responses to implanted Au-NWs show no overt reactive or toxic biological reactions besides those triggered by the injury itself. These results highlight the translational potential of Au-NWs electrodes for *in vivo* applications as neural interfaces in contact with central nervous tissues including the injured spinal cord.

1. Introduction

Neural electrical stimulation is emerging as a promising tool with an enormous therapeutic potential for the treatment of nervous system disorders, considered as one of the most prevalent causes of death and disability around the world [1,2]. Several clinical trials have already

* Corresponding author. Instituto de Ciencia de Materiales de Madrid, Consejo Superior de Investigaciones Científicas (ICMM-CSIC). Calle Sor Juana Inés de la Cruz 3, 28049, Madrid, Spain.
E-mail address: mc.terradas@csic.es (M.C. Serrano).
[1] ADB and JMR contributed equally to this work.

https://doi.org/10.1016/j.biomaterials.2021.121186
Received 21 June 2021; Received in revised form 5 October 2021; Accepted 12 October 2021
Available online 15 October 2021

provided useful insights into the utility of peripheral (*e.g.* NCT00387673 and NCT01628627) and central (*e.g.* NCT03465163) electrical stimulation [3], commonly using chemically stable and biocompatible platinum and platinum–iridium electrodes with low impedance (<10 kΩ) [4]. One successful example is the use of deep brain stimulation currently used in the clinics for epilepsy. Despite this promise, progress in the clinical application of neural recording and stimulation devices is still limited [5], mostly due to materials mismatch [6], including suboptimal engineering and inadequate interactions with biological environments *in vivo* triggering foreign-body responses. In this context, cell-non-invasive extracellular substrate-integrated microelectrode arrays (MEAs) are attracting much attention for the monitoring of neuronal functioning and connectivity routes of nervous nuclei and circuits [7,8]. In this context, gold (Au) has been, by far, one of the preferential materials for the design of neural electrodes due to its conductive, plasmonic and biocompatible properties [9,10]. Remarkably, the use of micro and nanoelectrodes based on Au has provided important advances to date to obtain higher quality and stability of neuronal recordings, as Spira and colleagues [11] and Dipalo et al. [12] have shown. More recently, Sasanpour and coworkers have used carbon nanotubes to improve electrical properties of Au microelectrodes [13].

The translation of neural interfaces to the clinical arena undoubtedly depends on new technologies operating at the nanoscale to better conform to the complexity of the functional components of our nervous system [5]. In this sense, nanotechnology has proved upgraded designs of materials to more accurately mimic the native extracellular environment and therefore attain a more intimate contact with individual neurons [14,15]. The miniaturization of electrodes for an operational localized stimulation has already been identified as a pivotal requirement for the optimization of neural interfaces, as nanometer scale electrodes enhance the precision of the stimulation and then optimize the efficiency of the stimulating devices [16]. Another remarkable breakthrough in this field was achieved with the demonstration that transistor arrays made of high-density silicon nanowires (NWs) could record signals from up to 50 different spatial positions in a single axon [17]. In addition, scalable intracellular electrodes based on vertical NWs made of a silicon core, encapsulated by a silicon dioxide shell and capped with a titanium/Au tip, were able to intracellularly record and stimulate neuronal activity from multiple neurons [18]. More recently, single-crystalline Au NWs enabled the recording of single-neuron activity in the live mouse brain with improved spatial resolution and differentiation of brain activity in response to different external behavioral stimuli such as intrusion [19]. In a multielectrode configuration, these Au NWs demonstrated diagnostic potential by registering and identifying the location of an epileptic seizure center. Indeed, vertical nanoscale structures support the growth of a variety of mammalian cells *in vitro*, besides being effective as eventual cell actuators [20]. Nanomaterials with optical, mechanoresponsive and magnetic properties are some of the very recent materials under investigation as more efficient platforms for neural recording and modulation [5]. Furthermore, nanowires-based structures are also showing promise as nanotools for neurodiagnostics [15], as in the case of ZnO NWs arrays on 3D graphene foams for the detection of Parkinson's disease biomarkers [21].

Despite all these remarkable contributions, little progress has been done to date on the understanding of the real impact that such neural interfaces have on neural network functionality. In previous work, we demonstrated that both chemical composition and nanotopography play pivotal roles in the *in vitro* interaction of metallic electrodes with cortical neural cells [22]. Under electrical stimulation, scattered Au-based nanostructured substrates composed of poorly ordered vertical NWs evoked intracellular calcium dynamics compatible with neural networks activation, thus highlighting the opportunity for using these electrodes to excite silent neural networks. Herein, we hypothesized that a higher ordered nanostructure could enhance the interaction with neural cells and tissues in a more efficient manner. Alumina-templated Au nanostructured electrodes were then proposed as useful candidates for both *in vitro* and *in vivo* applications in electrical stimulation. To further anticipate their impact in neural cells and tissues, we first challenged these substrates with primary neural cortical cells for up to 14 days *in vitro* (DIV) and analyzed major neural cell growth and network functioning parameters. We then proceeded to explore tissue responses to the subacute implantation of these nanostructured electrodes with NW arrays in the injured rat spinal cord foreseeing their impact on central neural tissues.

2. Results

2.1. Flexible Au nanostructured electrodes with a highly ordered network of vertical nanowires

Thin gold electrodes coated by a network of vertical NWs were prepared by template-assisted electrodeposition. Importantly, we used alumina (AAO) templates home prepared, which allowed gaining good control over the diameter, length and order of the NWs. Details on the electrode fabrication are provided in Materials and Methods. Fig. 1 shows a scanning electron microscopy (SEM) image in top view (panel A) and cross-section (panel B) of a representative Au nanostructured electrode (henceforth referred as Au-NWs electrode), after the removal of the AAO template. Closer details of the structure can be seen in corresponding insets. The figure shows that the electrode surface is fully coated by high-density (~109 NWs/cm^{-2}) and parallel NWs of 160 nm in diameter and 1.2 μm in length, arranged in a hexagonal disposition, with 320 nm of interdistance between NWs. These characteristics

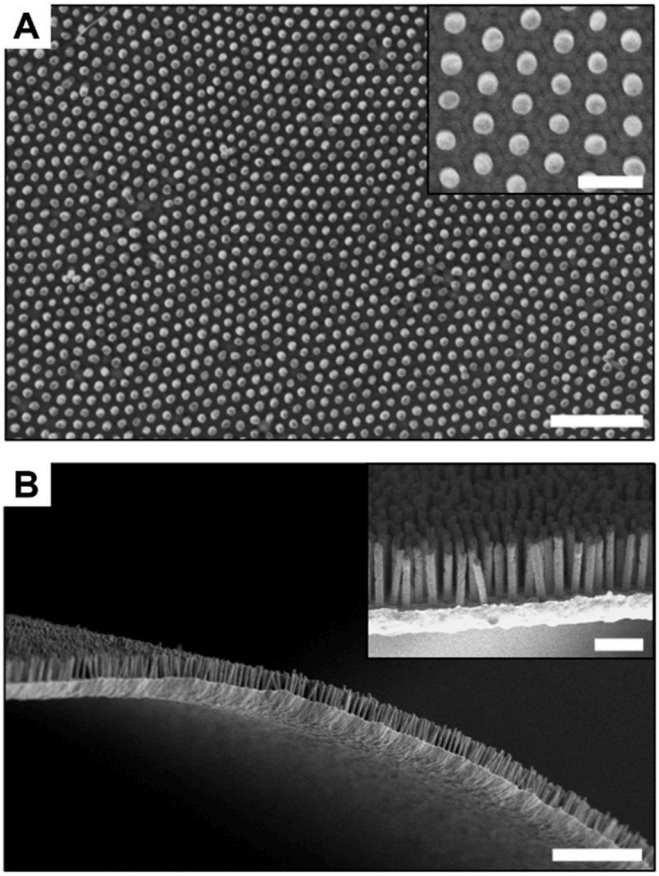

Fig. 1. SEM images of Au nanostructured electrodes obtained with AAO templates. Top (A) and cross-section (B) images showing an ordered network of parallel Au NWs of 1.2 μm in length and 160 nm in diameter standing over a flexible Au base. Scale bars: 2 μm (a), 0.5 μm (a-inset), 5 μm (b) and 1 μm (b-inset).

derived from the nanoporous pattern of the AAO templates. The Au-NWs array stand over an Au base of 0.5–1.0 μm in thickness. Equivalent plain electrodes without NW coating (Au-Flat) were also prepared for comparison (Figure S1A and S1C), as previously reported [22]. The entire Au-NWs electrode is flexible (Fig. 1B). Under manipulation, we observed no breakage, cracking or plastic deformation of the electrodes when they were bent down to a 0.5 mm curvature radius (Figure S1E). This flexibility can allow an easy adjustment of the electrodes to existing neural interfaces of different geometries.

The nanostructure of the Au-NWs electrodes translates in a larger actual effective area for a given geometric surface, which proportionally decreases the electrode impedance. To evaluate the increase in effective area of these Au-NWs electrodes, we recorded cyclic voltammograms of Au-NWs and Au-Flat electrodes of the same macroscopic size, ~0.13 cm^2 (Figure S2). Significantly, the Au-NWs voltammograms presents well outlined oxidation peaks characteristics of the oxide formation on different crystallography gold faces [23,24], in contrast to the broader peak observed for the smooth surfaces of the Au-Flat electrode [24,25]. We used the area of the gold reduction peak in the voltammograms to calculate the actual electrochemical effective area of the electrodes [26], and obtained values of 1.3 ± 0.18 cm^2 for Au-NWs electrodes and 0.20 ± 0.04 cm^2 for Au-Flat, where the errors are the standard deviation from at least 3 different samples. Therefore, the actual electrochemical area of Au-NWs electrodes is 6.5 ± 1.6 times larger than that of Au-Flat ones, in well agreement with the topography of the electrodes (a roughness factor of around 7 is expected for our NWs network in comparison with a completely flat surface). Then, we performed electrochemical impedance spectroscopy studies for both samples in phosphate buffer saline (PBS) and in the presence of bovine serum albumin (BSA; 0.2 mg mL^{-1}) (Figure S3). We observed that, in PBS, the impedance of the Au-Flat electrode was 6.6 times larger than that of the Au-NWs electrode (30.3 kΩ and 4.6 kΩ at 1 Hz, respectively), in perfect agreement with the lower effective area just described. In addition, we found that, when adding BSA, the impedance of the Au-Flat electrode increased ca. 2.2 times (up to 66.6 kΩ at 1 Hz), probably due to its adsorption on the electrode surface, while that of the Au-NWs electrode hardly varied, attesting the enhanced stability of our nanostructured electrodes.

Following Wenzel model [27], we expect this enhanced electrochemical area to translate into an improved wettability of Au electrodes, a relevant advantage to interface biological entities (*i.e.* dependent on aqueous media). We used water contact angle tests to study this effect. Observation proved that, while the contact angle for Au-Flat electrodes was of 47 ± 5°, Au-NWs electrodes displayed a super-hydrophilic behavior, with fast droplet spreading over the substrates and a minimal, or even not measurable, contact angle (Figure S1B and S1D). This result shows that air is not getting trapped within our nanostructure and water can penetrate among the NWs.

2.2. *Au nanostructured electrodes impact neural cell fate and sprouting in vitro*

Neural progenitor cells from embryonic cerebral cortices (NCCs) were isolated and cultured on Au-NWs electrodes. Bare flat and nanostructured electrodes displayed limited neural cell adhesion and development *in vitro* (Figure S4), so poly-L-lysine (PLL) coating, a conventionally used biological functionalization for neural cell culture [28,29], was selected to maximize neural cell colonization and survival. Morphological characterization by SEM demonstrated highly dense neural cultures formed on the NWs arrays after 14 DIV (Fig. 2A), with no apparent differences with respect to PLL-coated control glass substrates and non-nanostructured Au electrodes (Au-Flat) (Figure S5). More in detail, these primary neural cells were found to closely attach to the

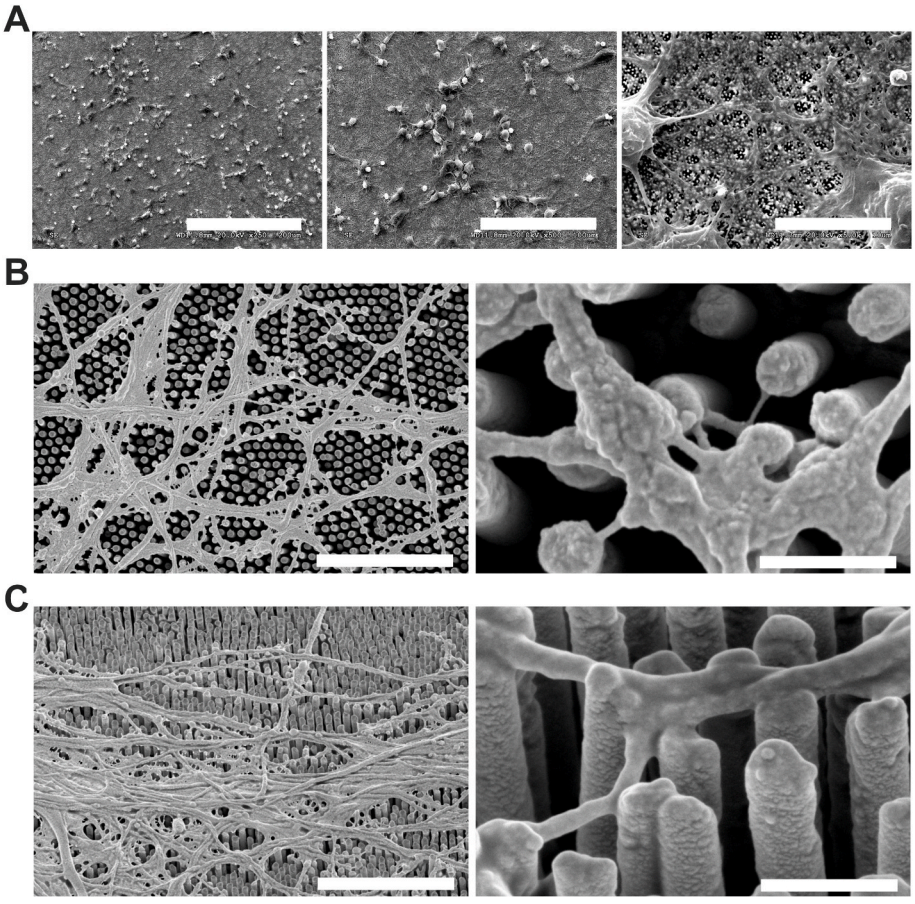

Fig. 2. Au nanostructured electrodes (Au-NWs) sustain the formation of highly dense primary neural cell cultures at 14 days *in vitro* when coated with low molecular weight PLL molecules. (A) Representative scanning electron microscopy images from cultures at high cell seeding conditions. Representative electron microscopy images from cultures at low cell seeding conditions on top (B) and 45° tilted (C) views. Scale bars: 200 μm (A, left), 100 μm (A, middle), 10 μm (A, right), 4 μm (B and C, left) and 400 nm (B and C, right).

nanowire-based topography of the arrays without signs of cell membrane piercing or perforation. Furthermore, these cells sprouted identifiable neurites mainly on top, but also on the lateral walls, of the NWs (Fig. 2B and C). We next examined neural cell viability by labelling live cells with calcein and dead cells with ethidium homodimer-1 (EthD-1). In accordance with electron microscopy results, cultures extensively colonized the totality of the array surface, revealing a majority of live cells, similarly to PLL-coated glass controls and Au-Flat counterparts (Fig. 3A). Quantitative examination of this data corroborated similar viability on these nanostructured electrodes with respect to both control substrates and flat electrodes, both in terms of the area occupied by live and dead cells (Fig. 3B) and the number of live cells per image field (Fig. 3C).

We next investigated the effect of these NWs arrays on the neural fate of these primary cells. On the one hand, neurons were identified by MAP-2 labeling, a microtubule-associated protein specifically abundant in mature neurons, while non-neuronal cells including glial cells were labeled for vimentin, a conventional cytoskeleton protein absent in neurons. Confocal microscopy images confirmed the formation of highly dense neural cultures covering the totality of the NWs arrays that were mainly composed by neurons (Fig. 4A). Quantitative studies evidenced significant differences in terms of the area occupied by neurons (Fig. 4B). Particularly, MAP-2$^+$ cells (neurons) on Au-NWs arrays covered a smaller area compared to glass substrates (one-way ANOVA, $p = 0.047$*), but not to flat counterparts. On the other hand, vimentin$^+$ cells (non-neuronal cells including astrocytes) covered similar areas among all three substrates (one-way ANOVA, $p = 0.718$). When focusing on the number of positive cells per field for both markers (Fig. 4C), the number of MAP-2$^+$ cells was statistically similar among substrates (one-way ANOVA, $p = 0.978$), while the number of vimentin$^+$ cells was significantly augmented on both Au-based electrodes with respect to glass coverslips (one-way ANOVA followed by Scheffé *post hoc* test; $p = 0.024$* control *vs* Au-Flat; $p < 0.001$*** control *vs* Au-NWs; $p = 0.009$** Au-Flat *vs* Au-NWs).

More specific features of neuronal growth were then investigated in search for the basis behind the significant reduction in the area occupied by MAP-2$^+$ cells on Au-NWs (with respect to control substrates) without changes in cell number. To do so, we focused on the morphology of MAP-2$^+$ cells (Fig. 5A). The number of first-order neurites per neuron was similar in neurons grown on Au-NWs with respect to control samples ($p = 0.074$), but significantly reduced in those on Au-Flat (one-way ANOVA followed by Games-Howell *post hoc* test; $p < 0.001$*** with respect to both control samples and Au-NWs) (Fig. 5B). To elucidate the potential impact of the isotropic architecture of Au nanostructured electrodes, we later analyzed the growth directionality of the neurites grown on the different substrates under investigation (Fig. 5C). No preferential growth directions were found in neurons cultured on either type of Au electrodes, neither in those cultured on control substrates. Based on these results, the slightly diminished area of MAP-2$^+$ cells found on Au-NWs could not be attributed to neither a reduction in the outgrowth of first-order neurites nor a developmental neurites polarization. A reduction in the number of second and third order neurites could account for the decreased MAP-2$^+$ area found.

2.3. *Au nanostructured electrodes facilitate spontaneous neuronal activity and rhythmicity in vitro*

Since glial cells are known to regulate synaptogenesis and control structural synapse formation, the increased number of vimentin$^+$ cells may indicate that Au substrates facilitate functional maturation of the cultured neurons. To explore this idea, NCCs cultured on Au-NWs for 14 DIV were loaded with the membrane permeable Fluo4-AM calcium dye to allow monitoring calcium transients (a hallmark of putative synapse formation and neuronal activity) in a population of neurons. In order to clearly identify the impact of nanostructure in the neuronal activity found, Au-Flat electrodes were also included in these studies and compared to glass coverslips (control). Spontaneous calcium transients were easily detected across the entire field of view and were strongly related to neuronal activity as shown by their abolishment in the presence of tetrodotoxin (TTX, 1 μM) used to block synaptic activity (Fig. 6A). Although much less frequent, glial transients were also observed as shown in a set of experiments in which SR101 was used to label glial cells (Figure S6A-B). These transients were easily identified by their increased amplitude, larger duration and slower rise slope and were excluded from this study (Figure S6C-D). By analyzing the amount of "active cells" (*i.e.* regions of interest, ROIs, showing at least one calcium event during the recording time), we found that both types of Au electrodes exhibited ~2.6-fold increase in the percentage of responding ROIs with respect to control samples (Fig. 6B and C). Raster plots of detected calcium transients were then computed to determine the Ca^{2+} event frequency (rate) and the inter-event interval (IEI) of neuronal activity. Interestingly, we observed that Au nanostructured electrodes, but not their flat counterparts, increased the frequency of neuronal events as shown by the averaged rate and the cumulative distribution of IEI (Fig. 6D and E). These results indicate that, although both types of Au electrodes improve neural activity, only those nanostructured increase the number of active regions and also their firing.

We next examined the kinetics of individual calcium events in terms of signal peak amplitude (ΔF/F), full-width half maximum (fwhm) and rise time (Fig. 6F and G). No differences were observed in the fwhm, indicating that neuronal activity tended to have the same duration in all conditions. The mean average of the rise time of the calcium events was

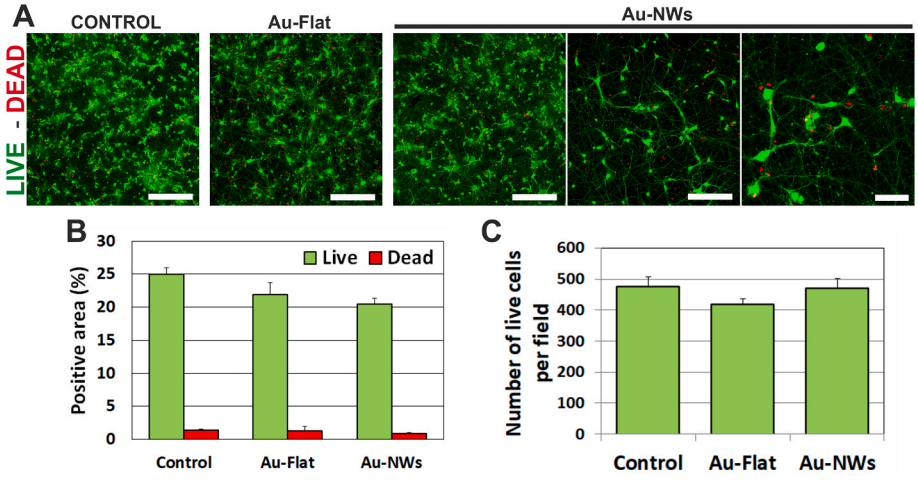

Fig. 3. Au nanostructured electrodes (Au-NWs) largely preserve primary neural cell viability after 14 days *in vitro*. (A) Representative fluorescence images of NCCs on Au-NWs at high (left) and low (middle and right) cell seeding conditions. Control substrates (glass) and Au-Flat electrodes at high cell seeding density are also shown for comparison. Live cells appear in green (calcein) and dead cells in red (EthD-1). Scale bars: 200 μm (control, Au-Flat and Au-NWs, left and middle) and 50 μm (Au-NWs, right). Quantitative viability results expressed as the area of positive staining (B) and the number of live cells (C). Statistics: one-way ANOVA. No statistically significant differences were found among groups. (For interpretation of the references to color in this figure legend, the reader is referred to the Web version of this article.)

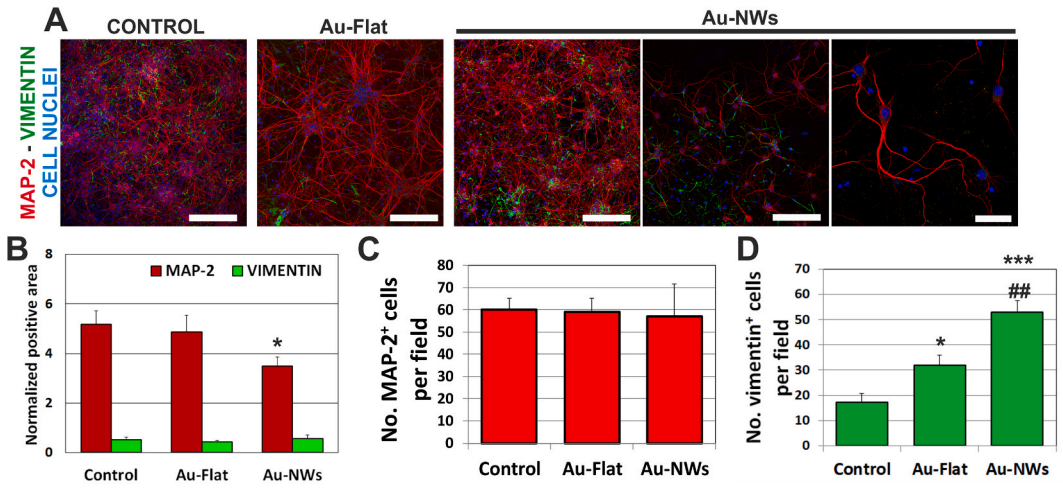

Fig. 4. Au nanostructured electrodes (Au-NWs) induce a preferential differentiation of primary neural cells to neurons and enhance their differentiation rate to glial cells with respect to control substrates (glass) and Au-Flat electrodes after 14 days *in vitro*. (A) Representative fluorescence images of NCCs on Au-NWs at high (left) and low (middle and right) cell seeding conditions. Control substrates and Au-Flat electrodes at high cell seeding density are also shown for comparison. Neurons appear in red (MAP-2^{+} labelling) and non-neural cells including glial cells in green (vimentin^{+}). Scale bars: 200 μm (control, Au-Flat and Au-NWs, left and middle) and 50 μm (Au-NWs, right). Quantitative neural differentiation results expressed as the normalized area of positive staining (B) and the number of MAP-2^{+} cells (C) and vimentin^{+} cells (D). Statistics: one-way ANOVA followed by either Scheffé or Games-Howell *post hoc* tests (as dictated by Levene's test). Significance: *$p < 0.05$ and ***$p < 0.005$ with respect to control samples; ##$p < 0.01$ with respect to Au-Flat. (For interpretation of the references to color in this figure legend, the reader is referred to the Web version of this article.)

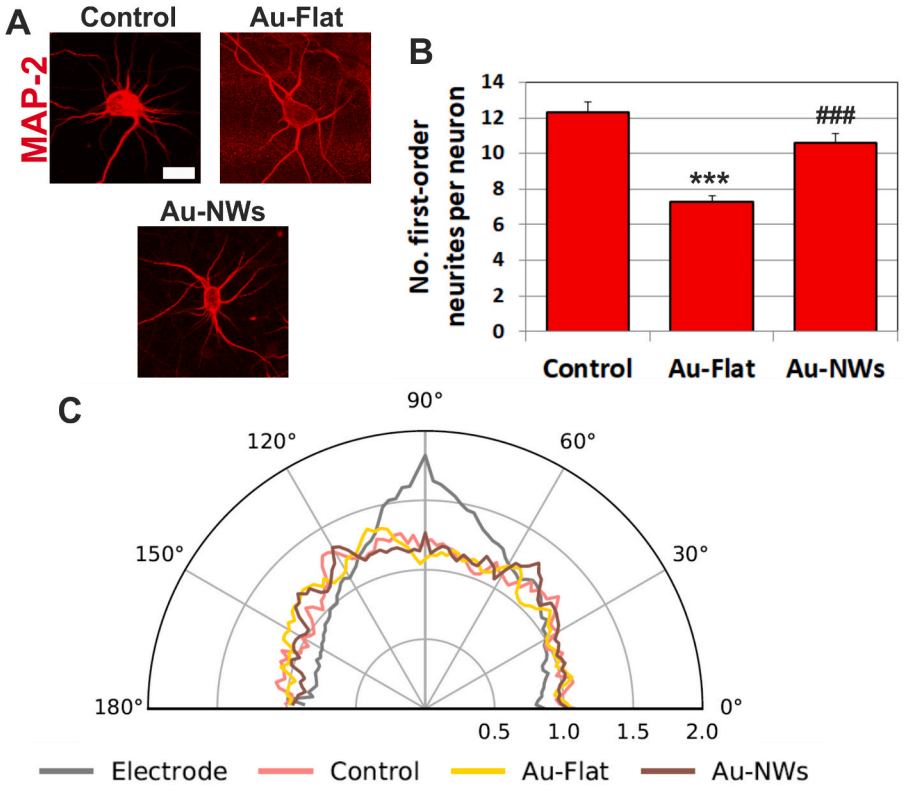

Fig. 5. Au nanostructured electrodes (Au-NWs) significantly increase the number of first-order neurites per neuron with respect to non-structured Au electrodes (Au-Flat), but have no impact on neurite spatial ordering after 14 days *in vitro*. (A) Representative immunofluorescence images of MAP-2^{+} neurons on control samples and Au-Flat and Au-NWs electrodes. Scale bar: 20 μm in all images. (B) Quantitative examination of the total number of first-order neurites per neuron. Statistics: one-way ANOVA followed by either Scheffé or Games-Howell *post hoc* tests (as dictated by Levene's test). Significance: ***$p < 0.005$ with respect to control samples and ###$p < 0.005$ with respect to Au-Flat. (C) Radial graph illustrating the directionality for Au-NWs electrodes prior cell culture (gray line) and for MAP-2^{+} cells grown on glass coverslips (control, pink), Au-Flat (yellow) or Au-NWs (brown). Please, note that the directionality degree results from NWs arrangement in the case of the bare electrodes (*i.e.* electrode), while it is mainly contributed by neural cell soma and neurites in the rest of cases (*i.e.* control, Au-Flat and Au-NWs). (For interpretation of the references to color in this figure legend, the reader is referred to the Web version of this article.)

also similar. However, its cumulative distribution showed a subpopulation of events on Au-NWs with faster responses. Finally, both Au-Flat and Au-NWs led to a significant decrease in the amplitude of the responses as shown by a left shift in the cumulative distribution of ΔF/F compared to control substrates. The observed changes in event kinetics might indicate that Au electrodes facilitate neuronal maturation and, therefore, neuronal connectivity. To further explore this hypothesis, we analyzed the degree of synchronization among neurons cultured on the different substrates to determine whether Au electrodes facilitated neuronal network. Visual inspections of raster plots and response histograms suggested that calcium events in Au-Flat and Au-NWs were more synchronous than in control conditions, as activity showed repetitive patterns and was clustered in narrow time windows (Fig. 7A). We then used cross-correlation analysis of Ca^{2+} transients from random

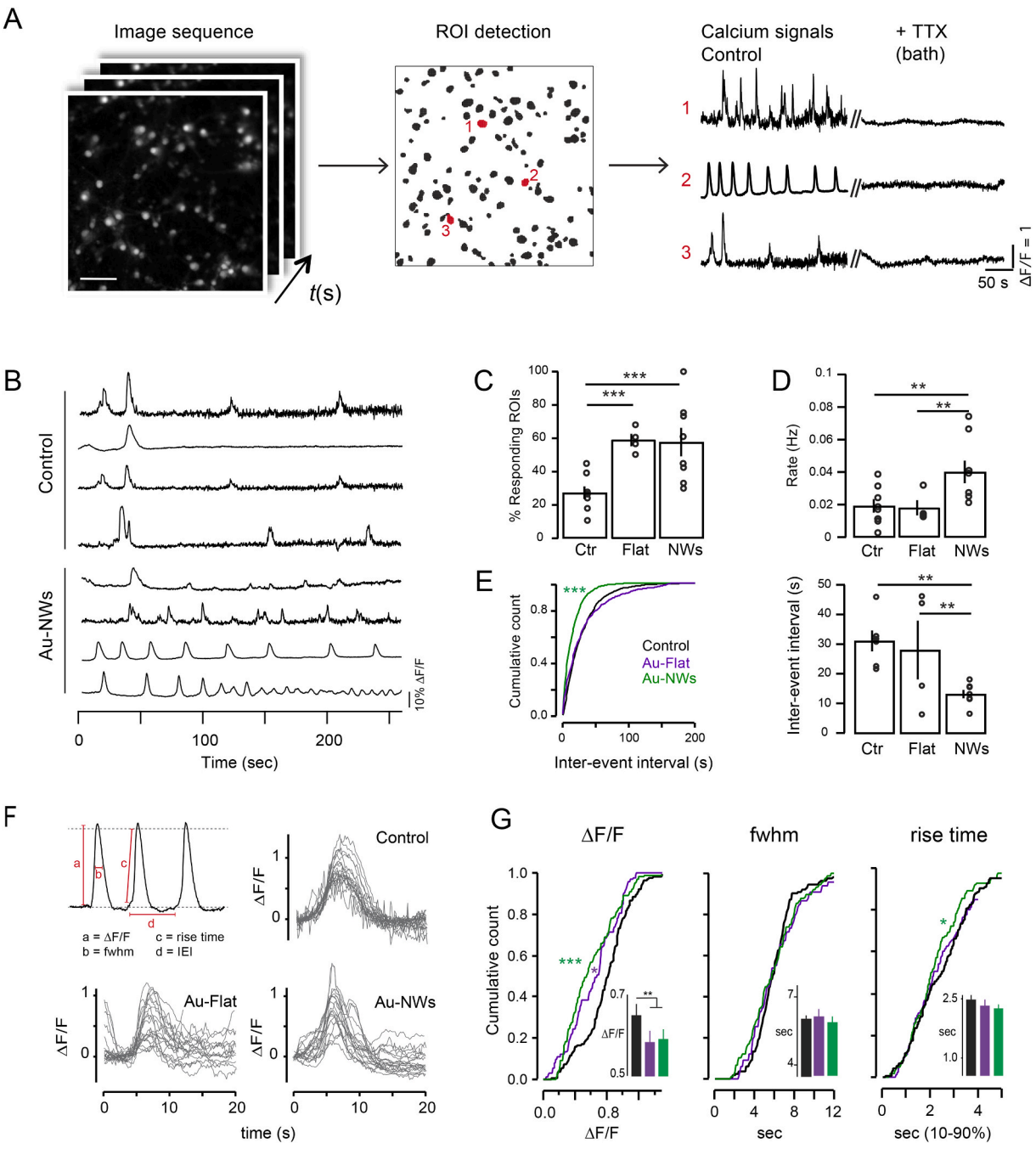

Fig. 6. Au nanostructured electrodes (Au-NWs) increase spontaneous Ca^{2+} activity in primary neural networks at 14 days *in vitro*. (A) Overview of image analysis showing the pseudo-automated segmentation performed to define regions of interest (ROIs). NCCs loaded with Fluo4-AM exhibited vivid spontaneous Ca^{2+} activity as shown by the representative fluorescence signals from the selected ROIs (red). The same ROIs are then showed with the fluorescence in time in the presence of tetrodotoxin (TTX, 1 μM) in bath solution. (B) Representative Fluo4-AM fluorescent traces obtained from neurons plated on either control substrates or Au-NWs. Averaged bar graphs showing the percentage of responding ROIs (C) and the rate of calcium events (D). (E) Left: Cumulative distribution of inter-event interval (IEI) in control (black), Au-Flat (purple) and Au-NWs (green) substrates. Right: averaged bar graphs of the IEI. (F) Representative trace showing the different parameters used in the kinetics analysis and overlapping of individual events taken from one representative experiment in each condition. (G) Cumulative distribution of the amplitude (ΔF/F), duration (fwhm) and rise time obtained from calcium events in control (black), Au-Flat (purple) and Au-NWs (green) substrates. Insets represent the mean average of the same values used for the cumulative distribution. Data collected from 2357 ROIs from 5 independent cell cultures for control samples, 929 ROIs from 3 independent cell cultures for Au-Flat and 1232 ROIs from 5 independent cell cultures for Au-NWs. Dots represent individual experiments. Data are expressed as the mean ± SEM. Statistics: one-way ANOVA followed by Tukey *post-hoc* or Kolmogorov-Smirnov tests. Significance: *$p < 0.05$, **$p < 0.01$ and ***$p < 0.001$. Please, refer to Figure S6 for further results on these studies. (For interpretation of the references to color in this figure legend, the reader is referred to the Web version of this article.)

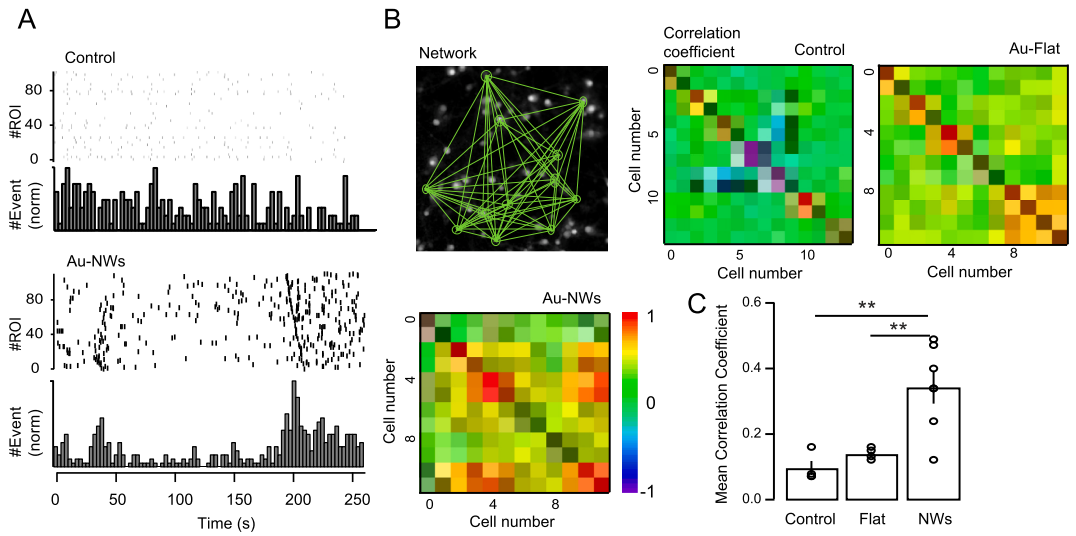

Fig. 7. Au nanostructured electrodes (Au-NWs) increase neuronal synchronization in primary neural cells after 14 days *in vitro*. (A) Representative raster plots of NCCs cultured on either control or Au-NWs substrates where each row represents Ca^{2+} events marked with black dots. Below each raster plot, the histogram shows the normalized sum of Ca^{2+} events in a 2-s window. (B) Exemplary network plot of random selected neurons. Heat-maps of the correlation coefficients between random selected neurons from one movie in each substrate. (C) Mean correlation coefficient of calcium transients in neurons cultured on Au-NWs, in comparison to control and Au-Flat substrates. Dots represent individual experiments. Data are expressed as mean ± SEM. Statistics: one-way ANOVA followed by Tukey *post hoc* test. Significance: **p < 0.01.

neurons within the field of view to determine the degree of neuronal synchrony (Fig. 7B). In control conditions, almost all cells exhibited asynchronous calcium transients as shown by the exemplary raster plot and the low value of the mean correlation coefficient (Fig. 7C). Interestingly, NCCs on both types of Au electrodes showed an increased pattern of synchronized activity, but also many individual activities. By comparing both types of Au electrodes, we found that Au-NWs facilitated even more the network among responding neurons as shown by the increased mean correlation coefficient. Altogether, our data indicates that Au electrodes facilitate neuronal activity by increasing the amount of neuronal cells showing spontaneous calcium events as well as their connectivity. In addition, Au nanostructured electrodes showed higher synchronized patterns of network activity suggesting a facilitation of neuronal maturation.

2.4. *Au nanostructured electrodes do not exacerbate inflammation when subacutely implanted at the injured spinal cord*

Encouraged by their positive effects on primary neural networks functioning *in vitro*, we then challenged Au nanostructured electrodes to interface central nervous tissue *in vivo*. Nanoelectrodes were implanted within the injured spinal cord and a proof-of-concept screening of their biocompatibility responses was carried out at 10 days post injury (DPI, subacute state). First, total body and major organs weights were examined in all injured animals (Table 1). Values from control rats (control) and injured rats without implant (injury) were also included for comparison. First, the total body weight of rats carrying the Au-NWs electrodes did not show statistically significant differences with respect to that of injured rats without implant at 10 DPI (one-way ANOVA followed by Scheffé *post hoc* test; p = 0.166). Regarding the liver, all injured rats displayed a significant increase of its relative weight with respect to control rats (p = 0.028*), although similar regardless the presence of the implant (p > 0.999). So, this significant hepatomegaly seems to be related to the injury itself, as previously reported [30,31], and not to the Au-NWs implantation. Neither the spleen (p = 0.059), the kidneys (p = 0.242) nor the lungs (p = 0.564) showed significant differences in their relative weights with respect to control and injured rats without implant.

We then focused on local responses of the injured spinal cord tissue

Table 1
Total body and major organs weight (in grams, g) from Au-NWs-implanted rats at 10 days post-injury (DPI). Absolute weight values are indicated in all cases. For each organ, relative values with respect to total body weight are also indicated between parentheses. Data are expressed as the mean ± standard deviation. Values from injured rats without implant are also shown for comparison. Statistics: one-way ANOVA followed by Scheffé *post hoc* test (as dictated by Levene's test). Significance: *p < 0.05 with respect to control rats.

Group	Body weight (initial)	Body weight (10 DPI)	Liver	Kidneys	Spleen	Lungs
Control	429 ± 5	–	13.05 ± 0.61 (3.05 ± 0.18)	2.48 ± 0.50 (0.58 ± 0.11)	0.72 ± 0.08 (0.19 ± 0.01)	2.51 ± 1.14 (0.66 ± 0.27)
Injury	457 ± 12	448 ± 23	16.74 ± 1.28 (3.73 ± 0.11) p = 0.028*	3.06 ± 0.19 (0.68 ± 0.06)	1.26 ± 0.26 (0.28 ± 0.05)	2.38 ± 0.32 (0.52 ± 0.04)
Au-NWs	430 ± 8	421 ± 13	15.68 ± 0.96 (3.73 ± 0.34) p = 0.028*	3.06 ± 0.31 (0.72 ± 0.06)	1.17 ± 0.11 (0.27 ± 0.02)	2.19 ± 0.35 (0.51 ± 0.08)

to the subacute implantation of Au nanostructured electrodes (Figure S7). We first evaluated the amount of cells populating the different regions of selection at the injured spinal cord. Cell nuclei were stained with Hoechst and the corresponding area occupied by them quantified as a univocal signature of cells presence (Fig. 8A). As expected from the inflammatory and scar pathways activated by the injury practiced, the interfaces, both caudal – CIF– and rostral – RIF–, and the epicenter of the lesion (where the Au-NWs electrodes array was implanted) experienced a marked increase in cell density (one-way ANOVA followed by Games-Howell; p < 0.001*** in all cases with respect to LH). Both CIF and RIF were similarly populated (p = 0.287). Moreover, regions slightly away from the lesion (PL12) showed no statistically significant differences with the left hemicord – LH (p > 0.999).

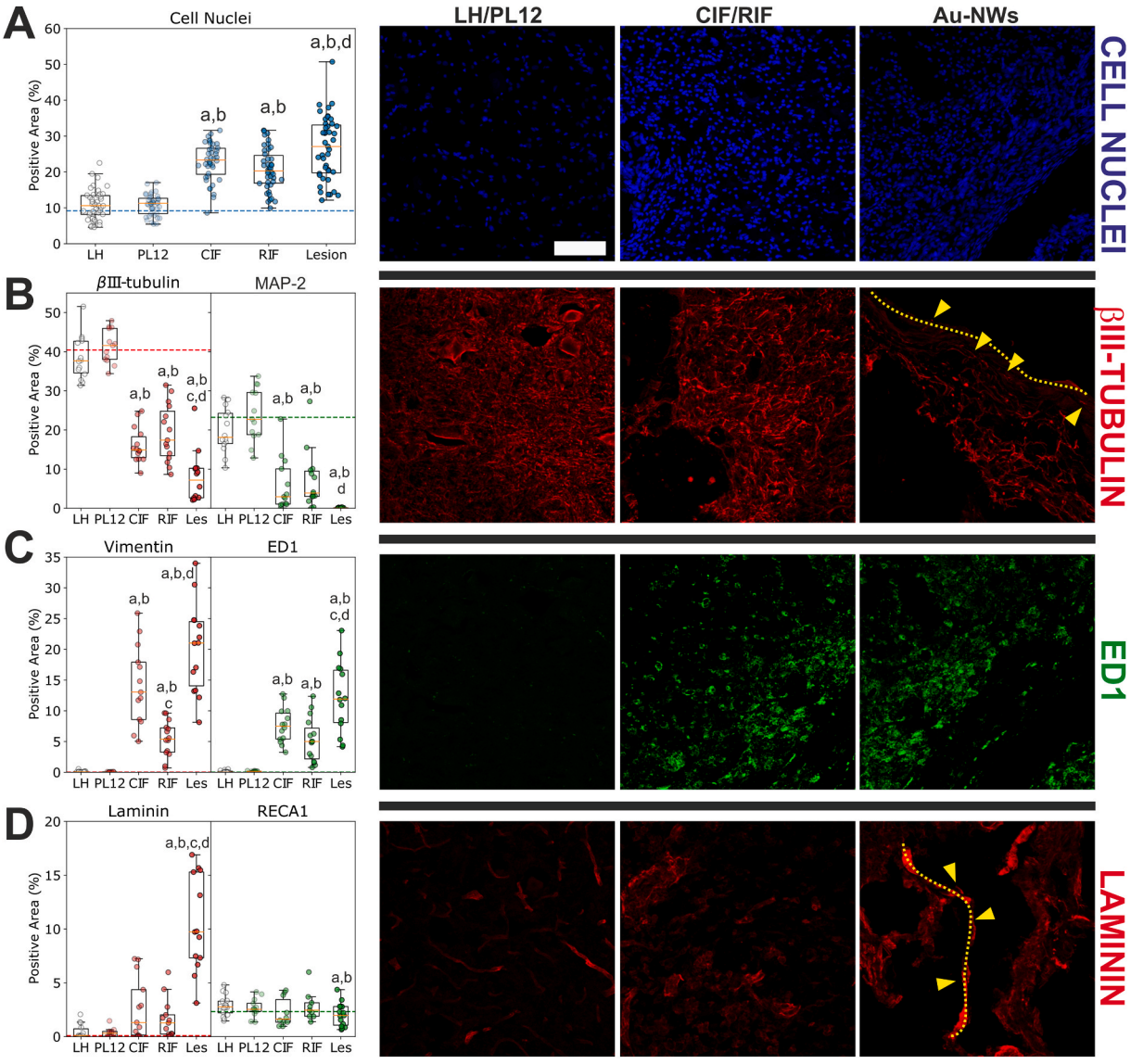

Fig. 8. Au nanostructured electrodes (Au-NWs) mediate favorable biocompatible responses when subacutely implanted in the injured rat spinal cord *in vivo*. Quantitative results (left) and representative immunofluorescence images (right) for the following markers: (A) cell nuclei, (B) βIII-tubulin (left graph and images) and MAP-2 (right graph), (C) vimentin (left graph) and ED1 (right graph and images), and (D) laminin (left graph and images) and RECA1 (right graph). Scale bar: 50 μm in all images. Statistics: one-way ANOVA followed by Games-Howell *post hoc* test (as dictated by Levene's test). Statistical significance with respect to LH (a), PL12 (b), CIF (c) and RIF (d) is indicated. For specific p values, please refer to the text and Table S1. Dashed lines in graphics correspond to mean values from control rats for each specific marker. CIF: caudal interface; Les: Lesion; LH: left hemicord; PL12: perilesional area at 1–2 mm; RIF: rostral interface. Positive elements in close contact with Au-NWs are indicated with yellow head arrows and the own Au-NWs implant with yellow dashed lines. (For interpretation of the references to color in this figure legend, the reader is referred to the Web version of this article.)

The lesion epicenter contained the highest value of total area occupied by cells, also significantly higher than RIF ($p = 0.002$***), but not than CIF ($p = 0.094$). We next investigated the specific effects of Au-NWs implantation on neuronal components by analyzing βIII-tubulin and MAP-2 (Fig. 8B). The injury practiced induced damage on neurons as demonstrated by the decreased number of both neuronal markers. Specifically, only PL12 remained similar to LH (one-way ANOVA followed by Games-Howell; $p = 0.805$ for βIII-tubulin and $p = 0.471$ for MAP-2), while the amount of βIII-tubulin and MAP-2 in the rest of regions were markedly reduced ($p < 0.001$*** in all comparisons with LH). Neuronal damage between interfaces was statistically similar ($p = 0.728$ for βIII-tubulin and $p = 0.995$ for MAP-2). Curiously, damage at MAP-2 elements was more profound at CIF, as this region became similar to the lesion site ($p = 0.055$). Nonetheless, this significant reduction of neuronal components related to the injury practiced did not avoid the observation of βIII-tubulin$^+$ components in close contact with Au-NWs (yellow head arrows in Fig. 8B). More importantly, when compared to injured rats without implant, there were not statistically significant differences in the reduction of neural components at any of the regions examined (Figure S8, Figure S9 and Table S1), thus proving that these nanostructured electrodes did not induce further damage to neural components than that associated with the injury itself when subacutely implanted *in vivo*.

The degree of tissue scarring and inflammation was next studied by analyzing the presence of vimentin and ED1 (Fig. 8C). Both markers behaved quite equally, thus being largely absent in LH and PL12 (one-way ANOVA followed by Games-Howell; $p = 0.536$ for vimentin and $p > 0.999$ for ED1) and significantly abundant at the interfaces and lesion

site ($p < 0.001$*** for all comparisons with respect to LH). The lesion site was, from them all, the region with the highest amount of vimentin$^+$ and ED1$^+$ cells, although CIF displayed a similar quantity of ED1$^+$ area ($p = 0.103$ with respect to lesion). Interestingly, CIF and RIF were comparably colonized by ED1$^+$ cells ($p = 0.309$), but not by vimentin$^+$ cells ($p = 0.003$***) as CIF had more area occupied by vimentin$^+$ components. When compared to injured rats without implant (Figure S8, Figure S9 and Table S1), only few statistically significant differences were identified. Specifically, the lesion epicenter in those rats receiving the Au-NWs implant was more significantly colonized by vimentin$^+$ cells ($p < 0.001$***). Although this result could be initially discouraging, a close inspection of the images clearly revealed a dramatic presence of cavities at the lesion site due to tissue retraction in those rats which were not implanted. These areas with no cell/tissue components were negligible in animals with Au-NWs electrodes, thus providing to the implant an additional and beneficial stabilization role at the lesion site. The presence of such cavities has been largely associated in the clinics with detrimental changes at the lesion site and beyond in patients [32–34]. In order to further characterize glial scar formation, we investigated the presence of glial fibrillary acidic protein (GFAP) and chondroitin sulphate glycosaminoglycans (CS56). Representative immunofluorescence images for the three experimental groups and different areas under study and respective quantification have been included in the supporting information (Figure S10 and Table S1). As could be observed, GFAP dramatically increased in all injured animals with respect to control (uninjured) ones ($p \leq 0.014$*, for all comparisons) in the areas under the influence of the lesion practiced (*i.e.* CIF, RIF and lesion epicenter). Regarding CS56, although its presence displayed a noticeable increase, differences with respect to control rats were not statistically significant ($p \geq 0.077$, for all comparisons). Importantly, both injured groups behaved similarly, without statistical differences between them in any of the areas studied for any of these two markers. Interestingly, the largest presence of astrocytes (GFAP$^+$ cells) were found at the interface tissue in both injured groups (being even more abundant at the rostral interface), while chondroitin sulphate glycosaminoglycans (CS56$^+$ components) seemed to be preferentially deposited at the very lesion site.

Finally, we focused on the presence of angiogenic features and vascular structures by staining laminin and RECA1 elements (Fig. 8D). On the one hand, laminin was slightly enhanced at the interfaces, but this increase was not statistically significant (one-way ANOVA followed by Games-Howell; $p = 0.109$ for CIF and $p = 0.223$ for RIF with respect to LH, $p = 0.083$ for CIF and $p = 0.144$ for RIF with respect to PL12). Moreover, both interfaces were comparably occupied by laminin ($p = 0.835$). On the contrary, the lesion site appeared significantly colonized by this protein ($p < 0.001$***), with evident laminin$^+$ components in close contact with the Au-NWs implant (yellow head arrows in Fig. 8D). When compared with injured rats not receiving the implant, only PL12 showed a slightly but significantly more abundant laminin content ($p = 0.038$*) in the presence of Au-NWs (Figure S8, Figure S9 and Table S1). Moreover, laminin at the lesion site differed more significantly from the rest of areas under study (*i.e.* LH, PL12, CIF and RIF) in Au-NWs-implanted rats than in those without the implant (only statistically significant for LH and PL12), although it was similarly present at the lesion site between both treatment groups ($p = 0.573$). On the other hand, RECA1 (an indicator of mature blood vessels) did not show significant differences in any of the areas under study ($p > 0.05$ in all comparisons), neither in comparison with control (uninjured) and injured rats without Au-NWs electrodes (Figure S8, Figure S9 and Table S1).

3. Discussion

Gold-based nanostructured electrodes combine two major features of interest for the design of neural interfaces with future value for the clinical diagnosis and treatment of neural disorders. On the one side, gold has been extensively proved as a biocompatible material with useful plasmonic and electrical properties for biomedical applications. On the other side, the incorporation of nanostructured clues is discovering a wide range of biological responses, including those from neural cells and tissues, being modulated in a customized manner. For instance, previous studies have shown that the use of Au nanostructures in the shape of MEAs reduce electrode impedance (15.4 ± 0.44 kΩ at 1 kHz) and favors an enhanced long-term stability of the electrode-neuron coupling due to the reduction of surrounding gliosis [35–37]. In general terms, vertical nanoscale structures efficiently support the growth of a diversity of mammalian cells, including neural cells [38]. For example, Raos and colleagues demonstrated that human neurons derived from a human teratocarcinoma cell line (hNT) were able to properly grow and remain functionally viable on individual florets composed of vertically-arranged ZnO NWs which were below 500 nm long [39]. Moreover, rat neuroblasts were successfully cultured on single vertical platinum NWs (1 μm in length; 50 nm in diameter) used for the detection of neuronal activity [40]. When in contact, cells tend to envelop these vertical structures, effectively adapting to their geometry, as herein described for NCCs in contact with Au-NWs.

Previous findings by our group proved the capacity of the nanostructured topography defined by NWs to increase cell survival, boost neuronal differentiation and reduce glial cells on Ni-NWs with respect to flat counterparts [22]. Differing from this former work with rather scattered NWs, herein, we investigated Au nanostructured electrodes fabricated by using home-prepared alumina templates, which provided a highly ordered and isotropic configuration of NWs, while allowing us to maintain a very similar NW diameter and length to those of our previous samples. Results from both confocal and electron microscopies showed highly dense and viable cultures of both neurons and glial cells covering the entire surface of the Au-NWs arrays. The area occupied by neurons (MAP-2$^+$ cells) slightly diminished on Au-NWs with respect to control substrates and flat counterparts, while no differences were found in the area covered by glial cells (vimentin$^+$ cells) between both types of Au-NWs (*i.e.* scattered *vs* densely packed NWs electrodes). Interestingly, in the present case of densely packed NWs electrodes, the number of glial cells, but not the area occupied by them, significantly augmented with respect to control glass substrates. This result opposes to that previously found by us with postnatal hippocampal cultures *in vitro* with scattered Au-NWs electrodes [22], or polymeric surfaces structured with nanopillars [41], as well as with other work from the literature [35]. When carefully comparing findings, major differences in electrode composition, fabrication methods and neural cells culture conditions clearly arise, thus justifying the biological disparity identified. For instance, in work by Chapman and colleagues [35], nanoporous gold (np-Au) biointerfaces were fabricated from Ag/Au alloys through traditional photolithography, deposition, and lift-off stages and patterned by photothermal annealing with a custom 532 nm continuous-wave laser. Interestingly, authors demonstrated that np-Au surfaces with small (≈30 nm) feature sizes decreased astrocyte coverage through the inhibition of the formation of focal adhesion areas. Contrarily, on np-Au surfaces with large (≈170 nm and greater) feature sizes, such mechanisms were less relevant but initial neuronal surface coverage was faster.

Neurons grown in culture develop extensive processes and form functional synaptic connections, providing an *in vitro* system to study activity of developing neurons. Ca^{2+} signaling is known to modulate several important phenomena during neural development such as specification of neuronal phenotype, neurite growth and cell cycle [42, 43]. Here, we applied optical recording of intracellular calcium transients to determine whether distinct Au electrode substrates would lead to alterations in the activity and network assembling of primary neural cells. We found that nearly 30% of control neural cells showed low frequency rate of uncorrelated, high-amplitude spontaneous activity. These features strongly differed when using Au substrates with a dramatic enhancement of regions of interests exhibiting spontaneous calcium events. In addition, NCCs grown in Au substrates containing a topographic surface like nanowires (Au-NWs) exhibited faster calcium

events in a much higher event rate. Our experiments also showed that the amplitude of neuronal calcium events was increasingly varied on Au electrodes. Such variability could be attributed to our segmentation method, which does not discriminate between soma and neurites, as well as pre- and post-synaptic sites known to exhibit distinct patterns of calcium transients [44,45]. However, together with the anatomical data and other functional features obtained in our study, we find very plausible that the decreased amplitude of calcium transients corresponds to ongoing processes of neuronal maturation, as previously shown. Organic calcium dyes as the one used in this study are non-linear and its fluctuation represents the amount of action potentials (APs) fired by an individual neuron. Therefore, small calcium transients represent either single APs or bursts of small number of APs, rather than subthreshold changes in the membrane potential. One characteristic change in the spatial and temporal properties of neuronal activity during maturation stages is a marked reduction of APs within bursts and a stabilization of neuronal activity levels in a synchronized manner. Therefore, although our results showing smaller amplitudes of calcium events should be interpreted carefully as variable Fluo-4-AM dye loading may account for some of that, it is plausible that Au-NWs are accelerating functional neuronal maturation leading to decreased amplitudes and rhythmic events [46,47]. Both changes in amplitude and synchronization have been related to the maturation of GABAergic synapses that serve to shunt excitation in order to control activity of glutamatergic neurons [46,48]. Although this is highly possible under our conditions, further studies to quantify excitatory and inhibitory synapses will be necessary to identify the molecular nature of this neuronal maturation.

Another evidence showing that Au-NWs promoted maturation is the increased ability observed by these primary neural cells to form local networks in order to synchronize and transfer information more efficiently [49,50]. Our data revealed that spontaneous Ca^{2+} activity in NCCs seeded on Au-NWs did not correspond to independent cell signals, but rather involved correlated activity, that is, higher connectivity between neurons. However, we postulate that enhanced synapse formation and connectivity may represent the mechanism behind the increased neuronal network. This is corroborated by our data showing that bath application of TTX completely blocked spontaneous calcium transients, thus indicating that calcium signals, and therefore network, were driven by functional synaptic activity. Although our study does not allow to discriminate whether maturation of functional networks on Au-NWs is due to either excitatory or inhibitory neurons, we assume that functional maturation is being largely mediated by presumptive glutamatergic neurons proved to assemble more efficient networks.

The favored functional neuronal networks (*i.e.* increased number of active cells and rhythmicity and higher ability for synchronization) found on Au-NWs could be, at least partially, attributed to the nanostructured features of these electrodes, based on the comparison with neural cell behavior on flat electrode counterparts (Au-Flat). In this sense, previous work in the literature demonstrated that electrodes with this type of nanoscale features managed to fix neural cells by forming a network of synaptic connections [7]. Using polymeric samples structured with nanopillars, we showed that the nanostructure itself enhances spontaneous neural activity and the degree of synchronization among cells pairs, independently of the conductive or insulating nature of the polymer [41]. Gautam and colleagues demonstrated that neurons were able to form functional networks when interfaced with vertically arranged indium phosphide NWs [51]. In fact, calcium imaging experiments performed with the Cal520-AM dye shown that the activity of these cells was highly correlated. In this case, calcium experiments were done by using hippocampal cells isolated from postnatal rodent pups to assure the presence of both neurons and glial cells. Two different kinds of activity were described for glial cells, corresponding to fast transients (rise time <0.5 s) and slow waves (rise time >2 s), whereas only one type of activity corresponded to neurons (fast transients with a rise time inferior to 0.25 s, likely corresponding to synaptic transmission). Moreover, in concordance with our results, burst of synchronized neuronal activity was detected in networks grown on the NWs, but not in cells grown on control glass coverslips (being the activity of glial cells also synchronized with neuronal activity). Indeed, the integration of the axon with the dendritic projections is likely promoted by the fact that the area of contact on the NWs surface is larger, thus achieving interconnections more similar to natural synapses in a 3D environment [52]. In our studies, the developmental degree of first-order neuronal neurites showed no differences in neurons grown on Au-NWs with respect to control substrates, so this parameter could be discarded as responsible for these functional differences. Contrarily, the amount of glial cells (*i.e.* vimentin^{+}), but not their associated area, denoted significant differences among substrates, being Au-NWs those with the highest quantity of glial cells. Despite the prevention of gliosis has been widely pursued in the design and *in vivo* application of neural interfaces, the occurrence of glial cells in neural cultures *in vitro* might be a positive feature enabling the attainment of more functionally efficient neural networks. This hypothesis finds sense on the well stablished definition of the tripartite synapsis, in which astrocytes are active partners in synapse functioning and signal transmission within the neural network [53,54]. Among other demonstrated functional roles, astrocytes experience calcium waves induced by glutamate released by neurons [55] and can mediate the potentiation of inhibitory synaptic transmission [56]. Calcium transients corresponding to glial cells observed in NCCs cultured on Au electrodes in these studies, although discarded from the analysis, are a proof of the functional state of glial cells on these NWs arrays. In the clinical scenario, this ability of Au-NWs to boost neuronal synchronization and network consolidation could assist mature neural networks stability by providing stabilization of remaining functional networks, reinforcing neural plasticity mechanisms and more efficiently influencing progenitors at the disturbed neural tissue. These hypotheses should be investigated in future work with an advanced version of our nanostructured devices to prove their relevance in future stimulation experiments. Moreover, the impact that the plasmonic properties of our Au-based electrodes could be having on these particular neural responses should be also unraveled.

These favorable effects of Au-NWs in neural cell cultures *in vitro* boosted our further interest in the evaluation of these nanostructured electrodes *in vivo*. Based on the eventual potential of these interfaces for therapeutic uses in central nervous tissues (*e.g.* electrical stimulation), we challenged the nanostructured electrodes by implanting them in the acute injured rat spinal cord approaching their eventual applicability as part of electrical stimulation devices for tetraplegic and paraplegic patients. We then evaluated their performance at the subacute stage in order to evidence early detrimental responses such as inflammatory and foreign body responses. First, systemic toxicity effects were investigated by looking for significant changes in major organs weight and macroscopic inspection, which were not detected. Second, local spinal tissue responses were screened by looking to specific neuronal, inflammatory and vascular markers. Although neuronal components (*i.e.* βIII-tubulin and MAP-2) were significantly diminished and inflammatory and glial scar formation signals enhanced (*i.e.* vimentin and ED1 and GFAP and CS56, respectively) at the lesion site and its vicinities, no major differences were found with respect to injured rats not receiving the Au-NWs implant. These results highlight the capacity of these interfaces to mediate biocompatible responses when in contact with injured central nervous tissues at the subacute stage. In line with these findings, Kang and colleagues hypothesized that the outstanding mechanical and electrical properties of single-crystal Au NWs could minimize the acute local trauma to brain tissue and increase the signal/noise ratio of recording, which can be both cited as the most remarkable advantages of these electrodes [19]. In a different study, Lu et al. fabricated flexible polymeric fibers coated with micrometer-thick meshes of silver NWs for neuronal stimulation and activity recording within the lumbar part (L1) of the spinal cord in mice [57]. Immunohistochemistry studies after 2 weeks of implantation by labeling of GFAP and NeuN showed imperceptible astrocyte proliferation and no tissue erosion in the surroundings

of the implant. Further *in vivo* studies at longer time points are needed to corroborate the favorable interaction of Au-NWs arrays with damaged central nervous tissues to boost their application *in vivo*. Moreover, specific experimental designs and electrical stimulation procedures based on the use of these arrays, and following guidelines recently published for soft electrode systems [58], will be explored.

4. Conclusions

We have designed highly ordered nanostructured electrodes composed of densely packed Au vertical NWs and explored their impact on primary neural cell cultures *in vitro* and spinal cord tissue *in vivo*. Au-NWs supported the growth of highly viable and dense neural cultures containing a majority of neurons accompanied by glial cells. By using live calcium imaging to study neuronal activity and network functioning, we found that flat and nanostructured Au electrodes facilitated neuronal responses by increasing the number of active cells and the rhythmicity of the events. In addition, our data showed a higher ability of neuronal synchronization when primary neural cells were seeded on Au-NWs, thus indicating that nanostructured features in these NWs electrodes favor neuronal network consolidation, which allows to efficiently transfer information more easily than flat electrodes. An enhancement in the number of glial cells and/or changes in neuron-dependent parameters could be behind these beneficial functional effects. Subacute responses to Au-NWs implanted in the injured rat spinal cord did not significantly differ from those induced by the injury itself, thus highlighting their potential for *in vivo* applications as neural interfaces in contact with central nervous tissues including the injured spinal cord.

5. Materials and methods

5.1. Materials

Chemical reagents and biological molecules were purchased from Sigma-Aldrich and used as received, unless otherwise indicated. Antibodies were bought from Sigma-Aldrich and Invitrogen. Neurobasal™ media and B-27 supplement were purchased from ThermoFisher. All materials and biological samples in this study were manipulated according to standard regulations so no safety concerns arise.

5.2. Fabrication and characterization of Au electrodes

Nanoporous anodic aluminum oxide (AAO) membranes were prepared by hard anodization of Al disks (Goodfellow, 99.999% in purity) under 140 V at 0–1 °C during 2.5 h in a water-based solution of oxalic acid ($C_2H_2O_4$, 0.3 M) and ethanol (0.9 M). The remaining Al was etched with an aqueous solution of $CuCl_2$ (0.1 M) and HCl (37%, 8.2 M). Finally, the oxide barrier was removed and the pores opened with an aqueous solution of H_3PO_4 (85%, 0.9 M) at 32 °C for 1 h and 50 min. We obtained AAO templates with ordered porous hexagonal pattern of ≈160 nm in diameter, 320 nm of interdistance and 109 cm^{-2} of pore density.

Nanostructured Au electrodes were prepared by template-assisted electrodeposition using these templates. We used similar conditions as described in our previous work [22]. After growth, the template was dissolved using an aqueous solution of CrO_3 (0.2 M) and H_3PO_4 (85%, 0.7 M) at 45 °C. The morphology of the arrays of metallic NWs was studied by SEM using a ZEISS EVO HD15 microscope and a SIGMA Field Emission SEM microscope. Wettability was evaluated by measuring the water contact angle using an Attention Theta, Biolin Scientific optical tensiometer. Cyclic voltammetry was carried out in a three-electrode cell. Silver paint was applied at the electrodes bottom to ensure a good electric contact with the cell working electrode. The measurements were performed in a N_2-saturated 0.5 M H_2SO_4 aqueous solution at room temperature. A PGSTAT204 potentiostat monitored by the NOVA software was used to cyclically swept the voltage from −0.2 V to 1.5 V (*vs.* Ag/AgCl), with a scan rate of 50 mV s^{-1}. At least three independent electrodes of each kind were tested. For the calculation of the actual electrochemical effective area from the reduction peak area, we took the broadly used value of 390 C cm^{-2} as the charge related to the reduction of one monolayer of gold oxide [26]. A slightly higher value of 448 C cm^{-2} has been also proposed as suitable for similar nanostructure gold surfaces [59]. Electrochemical Impedance Spectroscopy (EIS) studies was performed using a Metrohm Autolab PGSTAT204 potentiostat containing a specific FRA32 M module. Further details on these measurements have been provided in the supporting information.

Prior to cell culture, all electrode arrays were first fixed to glass coverslips with medical grade silicone to avoid flotation, then sterilized by UV radiation in a biosafety cabinet for 30 min and thereafter functionalized by adsorbing low molecular weight PLL molecules (30–70 kDa, 45 μg mL^{-1}, 1 h of incubation at room temperature). Glass coverslips were functionalized following the same protocol as for metallic electrodes and used as control substrates in all *in vitro* studies.

5.3. In vitro neural cell culture studies

Neural progenitor cells were obtained from cerebral cortices of Wistar rat embryos as previously described [60]. All the experimental protocols for cell collection adhered to the regulations of the European Commission (directives 2010/63/EU and 86/609/EEC) and the Spanish Government (RD53/2013 and ECC/566/2015) for the protection of animals used for scientific purposes. Adult female Wistar rats were provided by a commercial supplier (Harlan Ibérica, Spain) and sacrificed when gestation reached 16–17 days (E16-E17). At least 4 independent cultures with a minimum of 3 replicates per substrate condition in each culture were carried out ($N \geq 12$ arrays per type), except for live calcium dynamics studies in which a total of 10 cultures were performed. In all cases, the viability of the neural cells obtained was ≥85% after isolation. Electrode arrays were challenged to two different cell conditions: low ($2.5 \cdot 10^4$ cells) and high ($7.5 \cdot 10^4$ cells) cell seeding densities. Cells were maintained in complete Neurobasal™ media containing: B-27 supplement (2%), streptomycin (100 UI mL^{-1}), penicillin (100 UI mL^{-1}), and L-glutamine (1 mM) in a sterile incubator at 37 °C in a CO_2 atmosphere (5%). Culture media were half replaced every 3–4 days and cultures maintained for up to 2 weeks (14 DIV).

Cell culture morphology was first studied by electron microscopy. Briefly, culture samples were rinsed in PBS twice and fixed with glutaraldehyde (2.5% in PBS) for 45 min. After gentle washing in distilled water, dehydration was performed by using series of ethanol solutions for 15 min (2 washes) and a final dehydration in absolute ethanol for 30 min. Samples were then dried at room temperature for at least 48 h. After mounting in stubs and coating with a nanometer-thick Au layer under vacuum, the morphology of the samples was characterized by using a Hitachi S–3000 N and a last generation ultrahigh resolution FEI VERIOS 460 electron microscopes.

Cell viability was analyzed by using a Live/Dead® viability kit according to manufacturer's instructions (Invitrogen), based on the use of calcein and ethidium homodimer-1 (EthD-1). After staining, samples were visualized by using a Leica SP5 confocal laser scanning microscope. The fluorescence of both probes was excited by using an Argon laser tuned to 488 nm. After excitation, emitted fluorescence was separated by using a triple dichroic filter 488/561/633 and measured at 505–570 nm for green fluorescence (calcein) and 630–750 nm for red fluorescence (EthD-1). Physical reflection from the metallic electrodes (non-transparent) after excitation at 488 nm was also recorded and used to visualize the material structure and the relative cellular location.

Neural cell differentiation was investigated by immunofluorescence. Concretely, cultures were first fixed with paraformaldehyde (4% in PBS) at room temperature for 12 min and then incubated with primary antibodies against: (1) MAP-2 for somas and dendrites in neurons and (2) vimentin for non-neuron cells including glial cells. The secondary

antibodies used were: Alexa Fluor® 488 anti-mouse in goat IgG (H + L) and Alexa Fluor® 594 anti-rabbit in goat IgG (H + L) (Invitrogen). Both primary and secondary antibodies were dissolved in PBS containing saponin (0.25%) and fetal goat serum (2%) to guarantee cell permeability and to block any non-specific bindings, respectively. Each antibody was incubated for 1 h at room temperature in darkness. Cell nuclei were labeled with 4',6-diamidino-2-phenylindole (DAPI, 3 μM, 5 min). After immunostaining, samples were visualized by using a Leica TCS SP5 microscope. The fluorescence of the different fluorochromes was excited and measured as follows: Alexa Fluor® 488 excitation at 488 nm with an argon laser and detection at 507–576 nm, Alexa Fluor® 594 excitation at 594 nm with a helium-neon laser and detection at 625–689 nm and DAPI excitation at 405 nm with a diode UV laser and detection at 423–476 nm. Capture conditions in each case were stablished by using appropriate positive and negative controls and maintained during the acquisition of all the images. Reflection mode images were taken to observe the metallic electrodes surface in all cases.

For viability and differentiation studies, fluorescence images were acquired at 20X (775 × 775 μm^2). Higher magnification was only used to obtain qualitative detailed information from the images. The procedure used for the quantification of the positive labeled area for each marker was based on an automatized protocol (macro) created by using the Fiji software in which the observer must only define a threshold of positive staining for each marker stablished from the negative controls. The positively stained area for each particular marker was then expressed as a percentage of the total image area. Besides, the number of live, MAP-2^+ and vimentin$^+$ cells was also measured in each image by using the counter tool at the same Fiji software and used for comparison among substrates. Cultures at high cell seeding density conditions were used for these quantifications. Labelling of cell nuclei by Hoechst staining in differentiation studies assisted for the identification of individual cells during cell counting. MAP-2 images from differentiation studies at low cell seeding density were used for the quantification of first-order neurites in individual neurons. For spatial order studies, images acquired at reflection mode (for bare electrodes before neural cell culture) and MAP-2 images at high cell seeding conditions (for glass control, Au-Flat and Au-NWs) were analyzed by using the specific tool of directionality provided by the Fiji software and plotted in a radial graph (0° - 180°) (N ≥ 5 images for all substrates). In all cases, to minimize bias effects, quantifications were carried out blind by two independent observers.

5.4. In vitro calcium imaging acquisition and analysis

For calcium imaging, Fluo-4AM (Invitrogen F-14201) was dissolved in dimethyl sulfoxide to yield a 5 mM stock solution, which was further diluted in cultured medium to 5 μM. Coverslips containing NCCs were incubated with the probe at room temperature (21–24 °C) for 20–25 min. After that, coverslips were rinsed gently in culture media and then transferred to an immersion recording chamber where cells were constantly perfused with 95% O_2/5% CO_2 medium in a 2 mL/min flow. In a first set of experiments, Ca^{2+} transients were monitored using a Leica DMi8 S widefield epifluorescence microscope with incubation system for time-lapse studies, a Hamamatsu Flash 4 sCMOS digital camera for image detection and a 488 nm laser line. In a second set of experiments, Ca^{2+} transients were monitored using an ImagEM C9100-13 EMCCD camera (Hammamatsu) attached to an Olympus BX51WI microscope and illuminated with a CooLED pE-100 fluorescent excitation system. Images were acquired every 200 ms (5 Hz) using either the Leica DMi8 S or HCImage (Hamamatsu Inc) software under the control of pCLAMP10 (Molecular Devices, Inc). In some experiments, neuronal cultures were bath incubated with sulforhodamine 101 (SR101; 2 μM) for 5 min to label glial cells. Videos were analyzed offline using SARFIA (freely available on http://www.igorexchange.com/project/SARFIA), a suite of macros running in Igor Pro (Wavemetrics, Portland, OR) [61]. Prior to analysis, bleaching was corrected using exponential fitting in ImageJ and registered to correct movements in the X and Y directions if needed. Regions of activity (ROIs) containing both soma and neurites were chosen using a filtering algorithm based on a Laplace operator and segmented by applying a threshold, as described in detail elsewhere [62,63]. This algorithm defined most or all of the ROIs that an experienced observer would recognize by eye. Individual ROI responses were then normalized as the relative change in fluorescence (ΔF/F), smoothed by binomial Gaussian filtering, and analyzed to detect activity using custom-made scripts based on a first derivate detection algorithm. A threshold set at ~2 times the standard deviation of the time derivative trace was used to detect changes in fluorescence within the ROIs. The reliability of this algorithm to detect calcium activity was first tested by comparing the results with manual activity detection. In this work, the fluorescent intensity of ROIs is reported as the average intensity across all pixels within its area. Fluorescent responses are reported as normalized increases as follows:

$$\Delta F/F = (F - Fo)/Fo$$

where F is the instantaneous fluorescence induced by a spontaneous activity and Fo is the baseline fluorescence. Binary raster plots were then constructed from the detected events to analyze inter-event intervals (IEIs) and event rate. The time points in which calcium transients reach the threshold of the first derivative were also used to overlap individual calcium events used for the kinetics analysis. Rise time was defined as the time required going from 10 to 90% of the maximal amplitude and the full width half maximum (fwhm) was calculated at 50% of the maximal amplitude.

To study neuronal network, we used cross-correlation coefficients obtained by calculating the zero-lag pairwise Pearson correlation coefficients of neuron *i* and neuron *j* using the Matlab corrcoef routine (MathWorks, Inc). The resulting matrix of cross-correlation coefficients for spontaneous activity was clustered using hierarchical clustering with maximum or complete-linkage clustering. Cross-correlation matrices were plotted without rearranging the neurons and the average of the mean correlation coefficient obtained.

5.5. In vivo implantation studies at the injured rat spinal cord

Adult male Wistar rats were provided by a commercial supplier (Janvier Labs, France) and used at the age of *ca.* 12 weeks. The lesion model of choice was a right lateral hemisection at C6 segment, rostral to the bulk of *triceps brachi* motoneurons, as a suitable model to evaluate therapeutic strategies aimed at promoting neural plasticity and repair [64]. All the experimental protocols for surgical scaffold implantation at the spinal cord adhered to the regulations of the European Commission (directives 2010/63/EU and 86/609/EEC) and the Spanish government (RD53/2013 and ECC/566/2015) for the protection of animals used for scientific purposes. Treatment groups included: control (no surgery; N = 3), injured rats (hemisection at C6 without implantation of any material; N = 3) and Au-NWs rats (hemisection at C6 with implantation of a non-PLL-coated Au-NWs electrodes array; N = 3). Rats were housed at a 12 h light/dark cycle with food and water *ad libitum*. All surgical procedures were performed under intraperitoneal (IP) analgesia with xylacine (10 mg kg^{-1}) and anesthesia with sodium pentobarbital (55 mg kg^{-1}) mixed with atropine (0.05 mg kg^{-1}). Eyes were covered with Lubrithal™ gel to prevent corneal abrasion and dehydration. Temperature, color and respiratory frequency were constantly monitored during the complete surgical procedure. A midline incision was performed on the dorsal skin from the base of the skull up to the T3 backbone level. Superficial and deep muscles were carefully dissected, always along the midline. Vertebrae insertions of deeper muscles were cut at both sides of the spinal processes to get access to the backbone (typically from C4 to T2). After thorough identification, C5 vertebra was removed and the meninges visualized. A square incision was practiced on the dura mater to completely expose the spinal cord at C6 level. By using appropriate micro-scissors, one firm cut was then carried out at C6 to achieve a right

lateral hemisection. Bleeding was quickly contained by using small sterile pieces of Spongostan®. Au-NWs arrays, without PLL coating, were then implanted inside the spinal cut created. Superficial and deep muscles were smoothly approximated with a 3/0 synthetic absorbable sterile surgical suture (Coated VICRYL®), also used to close the skin. A plastic bandage (Nobecutan®) was finally sprayed on the sutured area to facilitate healing and avoid infection. The immediate post-operatory care protocol included subcutaneous administration of antibiotics (enrofloxacine 2.5%, 0.3 mL kg^{-1} every 24 h), analgesia (meloxicam 5 mg mL^{-1}, 0.1 mL kg^{-1}, every 12 h) and saline solution (NaCl 0.9%, 5 mL, once or twice a day depending on the hydration state of the animal) during the first three days. Posteriorly, animals were frequently observed with major attention placed into signs of pain, distress, dehydration, intestinal obstruction, and respiratory failure. At 10 DPI, animals were sacrificed by using a standard perfusion-fixation protocol and the spinal cords were extracted. Major organs (*i.e.* liver, kidneys, spleen and lungs) were extracted for macroscopic inspection and weight change evaluation.

5.6. Spinal tissue processing and immunofluorescence studies

All perfused spinal cord samples were placed in paraformaldehyde (4% in PBS) at 4 °C overnight and then 3 days in sucrose (30% in PBS) at 4 °C for cryo-protection. Tissue pieces were mounted on plastic containers, quick-frozen in Optimal Cutting Temperature compound (Tissue Tek, Hatfield, PA) and cut in horizontal sections of 10-μm by using a Leica CM1900 cryostat with an angle of 10°. The entire C5–C7 fragment was cut in sagittal sections from right to left. Spinal cord samples were examined for the presence of the following markers: (1) MAP-2 for somas and dendrites in neurons, (2) vimentin for non-neuron cells including glial and connective tissue cells, (3) ED1 for macrophages, (4) β-III tubulin for cytoskeleton microtubules in neurites, (5) GFAP for astrocytes, (6) CS56 for chondroitin sulphate glycosaminoglycans, (7) RECA-1 for endothelial cells in blood vessels, and (8) laminin for basement membranes in blood vessels. Appropriate secondary antibodies were selected accordingly. In all cases, cell nuclei were visualized by labeling with Hoechst (1 mg mL^{-1}). Fluorescence images were collected by using a Leica TCS SP5 microscope. Capture conditions were fixed by using sections from the three experimental groups incubated with the secondary antibodies but without the primary ones. All images were thereafter acquired under these conditions. All fluorescence images were automatically quantified by using a customized macro in Fiji software as the number of pixels (correspondent μm^2) positively stained for each particular fluorescence marker after the definition of the correspondent threshold of positive labeling. Control spinal cords and the contralateral hemicord in injured animals served as reference values to define correspondent threshold values for each marker. At least three non-overlapping images per animal were acquired in each position of interest ($N \geq 9$ per fluorescence marker, study region and group from 3 different animals per group). Areas under study were: left hemicord –LH–, perilesional areas at 1–2 mm from the lesion site –PL12–, caudal interface of the lesion – CIF–, rostral interface of the lesion– RIF–, lesion site without scaffold (injured animals without implant), and lesion site with Au-NWs implant. Additional bright field images were taken to define electrode location.

5.7. Statistics

In vitro viability, differentiation and calcium dynamics values are expressed in conventional bar graphs as the mean ± standard error of the mean (SEM), unless otherwise indicated, of at least three independent experiments ($N \geq 3$). *In vivo* immunofluorescence data from a total of three different animals ($N = 3$) are graphed as box plots, the orange line inside corresponding to the mean of the distribution. The top and bottom of the box represent, respectively, the 75th and 25th percentiles. The whiskers out of the box denote the range of outer-most data that fall within 1.5 x interquartile range. Additionally, single data points were overlapped with their correspondent box plots. Statistical analysis was performed by using the Statistical Package for the Social Sciences (SPSS, version 17.0). Comparisons among groups were done by one-way analysis of variance (ANOVA) followed by either *post-hoc* Scheffé or Games-Howell tests (homogeneous *vs.* heterogeneous variances, respectively, as dictated by Levene's test); except for calcium dynamics in which the *post-hoc* Tukey's test was selected. Comparisons between two groups were carried out by *T* test. In calcium studies, differences among cumulative distributions were evaluated using the Kolmogorov-Smirnov test. In all cases, the significance level was defined as $p < 0.05$.

Supporting information

Contact angle and bending results for Au-Flat and Au-NWs electrodes. Representative cyclic voltammograms for Au-Flat and Au-NWs electrodes. EIS methodological details and results for Au-Flat and Au-NWs electrodes. Morphological SEM examination of NCCs cultures on bare electrodes. Morphological SEM examination of NCCs cultured on control glass substrates and Au-Flat electrodes. Glial calcium transients on Au-NWs. Representative merged immunofluorescence images of spinal cord tissue after subacute Au-NWs implantation (10 DPI). Representative merged immunofluorescence images of spinal cord tissue from injured rats without implant (10 DPI). Quantitative data corresponding to spinal cord tissue immunofluorescence studies in control and injured rats without electrode implants. Representative merged immunofluorescence images and respective quantitative data for GFAP and CS56 of spinal cord tissue from the three experimental groups at 10 DPI. Table S1 summarizing *p* values for all immunofluorescence markers from statistical comparisons of tissue responses after Au-NWs implantation with respect to control and injured rats without implant.

Funding sources

This work was funded by the European Union's Horizon 2020 research and innovation programme under grant agreement No. 737116. It was also partially funded by the European Union's Horizon 2020 research and innovation programme under the Marie Sklodowska-Curie grant agreement No. 794926 (JMR), the Spanish MICINN under RYC2019-026870-I (JMR), project BiSURE (DPI2017-90058-R; MTG) and the 'Severo Ochoa' Programme for Centres of Excellence in R&D (SEV-2016-0686; RM), as well as by the *Comunidad de Madrid* through the project NanoMagCOST (CM S2018/NMT-4321; RM).

Author credit statement

BLR, AAN, PO, MTG and LP: Electrodes fabrication and characterization. ADB, AGM, ELD and MCS: Performed all *in vitro* and *in vivo* studies. EBM: Participated in *in vitro* studies and contributed to data analysis. ADB, JMR, JA and MCS: Specifically designed and carried out *in vitro* calcium studies and their data analysis. MTG, LP, ELD, JC, RM and MCS: Conceptualization. All authors: Manuscript writing and revision. Final version of the manuscript approved by all authors.

Data availability

All raw and processed data required to reproduce these findings will be available to download from DIGITAL.CSIC upon acceptance.

Declaration of competing interest

The authors declare that they have no known competing financial interests or personal relationships that could have appeared to influence the work reported in this paper.

Acknowledgment

Authors are thankful to the *Servicio Interdepartamental de Investigación* at the *Universidad Autónoma de Madrid* for assistance with scanning electron microscopy studies. The Advanced Light Microscopy Service at the *Centro Nacional de Biotecnología* (CNB–CSIC) and the Service of Microscopy and Image Analysis at the HNP are acknowledged for assistance with CLSM studies. Authors are grateful to Dr. André Espinha for his assistance with graphs and figure preparation. We also acknowledge the service from the MiNa Laboratory at IMN and funding from CM (project SpaceTec, S2013/ICE2822), MINECO (project CSIC13-4E-1794) and EU (FEDER, FSE). BLR acknowledges UCM for her predoctoral fellowship.

Appendix A. Supplementary data

Supplementary data to this article can be found online at https://doi.org/10.1016/j.biomaterials.2021.121186.

References

[1] S. Nag, N.V. Thakor, Implantable neurotechnologies: electrical stimulation and applications, Med. Biol. Eng. Comput. 54 (2016) 63–76, https://doi.org/10.1007/s11517-015-1442-0.
[2] J.S. Perlmutter, J.W. Mink, Deep brain stimulation, Annu. Rev. Neurosci. 29 (2006) 229–257, https://doi.org/10.1146/annurev.neuro.29.051605.112824.
[3] Last retrieved, https://www.clinicaltrials.gov/ct2/home. (Accessed 4 October 2021).
[4] S.F. Cogan, Neural stimulation and recording electrodes, Annu. Rev. Biomed. Eng. 10 (2008) 275–309, https://doi.org/10.1146/annurev.bioeng.10.061807.160518.
[5] R. Chen, A. Canales, P. Anikeeva, Neural recording and modulation technologies, Nature Rev 2 (2017) 16093, https://doi.org/10.1038/natrevmats.2016.93.
[6] V.S. Polikov, P.A. Tresco, W.M. Reichert, Response of brain tissue to chronically implanted neural electrodes, J. Neurosci. Methods 148 (2005) 1–18, https://doi.org/10.1016/j.jneumeth.2005.08.015.
[7] M.E. Spira, A. Hai, Multi-electrode array technologies for neuroscience and cardiology, Nat. Nanotechnol. 8 (2013) 83–94, https://doi.org/10.1038/nnano.2012.265.
[8] M.E. Spira, N. Shmoel, S.-H. Huang, H. Erez, Multisite attenuated intracellular recordings by extracellular multielectrode arrays, a perspective, Front. Neurosci. 12 (2018) 212, https://doi.org/10.3389/fnins.2018.00212.
[9] D. Brüggemann, B. Wolfrum, V. Maybeck, Y. Mourzina, M. Jansen, A. Offenhäusser, Nanostructured gold microelectrodes for extracellular recording from electrogenic cells, Nanotechnology 22 (2011) 265104, https://doi.org/10.1088/0957-4484/22/26/265104.
[10] R. Damnjanovic, P. Bazard, R.D. Frisina, V.R. Bhethanabotla, Hybrid electro-plasmonic neural stimulation with visible-light-sensitive gold nanoparticles, ACS Nano 14 (2020) 10917–10928, https://doi.org/10.1021/acsnano.0c00722.
[11] A. Hai, J. Shappir, M.E. Spira, Long-term, multisite, parallel, in-cell recording and stimulation by an array of extracellular microelectrodes, J. Neurophysiol. 104 (2010) 559–568, https://doi.org/10.1152/jn.00265.2010.
[12] M. Dipalo, H. Amin, L. Lovato, F. Moia, V. Caprettini, G.C. Messina, F. Tantussi, L. Berdondini, F. De Angels, Intracellular and extracelular recording of spontaneous action potentials in mammalian neurons and cardiac cells with 3D plasmonic nanoelectrodes, Nano Lett. 17 (2017) 3932–3939, https://doi.org/10.1021/acs.nanolett.7b01523.
[13] M. Vafaiee, R. Mohammadpour, M. Vossoughi, E. Asadian, M. Janahmadi, P. Sasanpour, Carbon nanotube modified microlectrode array for neural interface, Front. Bioengineer. Biotechnol. 8 (2021) 582713, https://doi.org/10.3389/fbioe.2020.582713.
[14] S.K. Seidlits, J.Y. Lee, C.E. Schmidt, Nanostructured scaffolds for neural applications, Nanomedicine 3 (2008) 183–199, https://doi.org/10.2217/17435889.3.2.183.
[15] D. Suradip, A. Carnicer-Lombarte, J.W. Fawcett, U. Bora, Bio-inspired nano tools for neuroscience, Prog. Neurobiol. (N. Y.) 142 (2016) 1–22, https://doi.org/10.1016/j.pneurobio.2016.04.008.
[16] G.M. Dittami, R.D. Rabbitt, Electrically evoking and electrochemically resolving quantal release on a microchip, Lab Chip 10 (2010) 30–35, https://doi.org/10.1039/B911763F.
[17] F. Patolsky, B.P. Timbo, G. Yu, Y. Fang, A.B. Greytak, G. Zheng, C.M. Lieber, Detection, stimulation, and inhibition of neuronal signals with high-density nanowire transistor arrays, Science 133 (2006) 1100–1104, https://doi.org/10.1126/science.1128640.
[18] J.T. Robinson, M. Jorgolli, A.K. Shalek, M.H. Yoon, R.S. Gertner, H. Park, Vertical nanowire electrode arrays as a scalable platform for intracellular interfacing to neuronal circuits, Nat. Nanotechnol. 7 (2012) 180–184, https://doi.org/10.1038/nnano.2011.249.
[19] M. Kang, S. Jung, H. Zhang, T. Taejoon Kang, H. Kang, Y. Yoo, J.-P. Hong, J.-P. Ahn, J. Kwak, D. Aejong Jeon, N.A. Kotov, B. Bongsoo Kim, Subcellular neural probes from single-crystal gold nanowires, ACS Nano 8 (2020) 8182–8189, https://doi.org/10.1021/nn5024522.
[20] A.F. McGuire, F. Santoro, B. Cui, Interfacing cells with vertical nanoscale devices: applications and characterization, Annu. Rev. Anal. Chem. 11 (2018) 101–126, https://doi.org/10.1146/annurev-anchem-061417-125705.
[21] H.Y. Yue, S. Huang, J. Chang, C. Heo, F. Yao, S. Adhikari, F. Gunes, L.C. Liu, T. H. Lee, E. Oh, B. Li, J.J. Zhang, T.Q. Huy, N. Luan, Y.H. Van Lee, ZnO nanowire arrays on 3D hierarchical graphene foam: biomarker detection of Parkinson's disease, ACS Nano 8 (2014) 1639–1646, https://doi.org/10.1021/nn405961p.
[22] A. Domínguez-Bajo, B.L. Rodilla, I. Calaresu, A. Arché-Núñez, A. González-Mayorga, D. Scaini, L. Pérez, J. Camarero, R. Miranda, E. López-Dolado, M. T. González, L. Ballerini, M.C. Serrano, Interfacing neurons with nanostructured electrodes modulates synaptic circuit features, Adv. Biosystems (2020) 2000117, https://doi.org/10.1002/adbi.202000117.
[23] A. Hamelin, Cyclic voltammetry at gold single-crystal surfaces. part 1. behaviour at low-index faces, J. Electroanal. Chem. 407 (1996) 1–11, https://doi.org/10.1016/0022-0728(95)04499-X.
[24] C. Jeyabharathi, P. Ahrens, U. Hasse, F. Scholz, Identification of low-index crystal planes of polycrystalline gold on the basis of electrochemical oxide layer formation, J. Solid State Electrochem. 20 (2016) 3025–3031, https://doi.org/10.1007/s10008-016-3228-1.
[25] C. Jeyabharathi, U. Hasse, P. Ahrens, F. Scholz, Oxygen electroreduction on polycrystalline gold electrodes and on gold nanoparticle-modified glassy carbon electrodes, J. Solid State Electrochem. 18 (2014) 3299–3306, https://doi.org/10.1007/s10008-014-2657-y.
[26] S. Trasatti, O.A. Petrii, Real surface area measurements in electrochemistry, J. Electroanal. Chem. 327 (1992) 353–376, https://doi.org/10.1016/0022-0728(92)80162-W.
[27] R.N. Wenzel, Resistance of solid surfaces to wetting by water, Ind. Eng. Chem. 28 (1936) 988–994, https://doi.org/10.1021/ie50320a024.
[28] R. Hrostkorte, M. Schachner, J.P. Magyar, T. Vorherr, B. Schmitz, The fourth immunoglobulin-like domain of ncam contains a carbohydrate recognition domain for oligomannosidic glycans implicated in association with l1 and neurite outgrowth, J. Cell Biol. 121 (1993) 1409–1421, https://doi.org/10.1007/BF01209947.
[29] J.A. Colombo, J.I. Almeida, S. Molina, In vitro culture and labeling of neural cell aggregates followed by transplantation, Exp. Neurol. 98 (1987) 606–615, https://doi.org/10.1016/0014-4886(87)90269-X.
[30] A.D. Sauerbeck, J.L. Laws, V.V.R. Bandaru, P.G. Popovich, N.J. Haughey, D. M. McTigue, Spinal cord injury causes chronic liver pathology in rats, J. Neurotrauma 32 (2015) 159–169, https://doi.org/10.1089/neu.2014.3497.
[31] X. Sun, Z.B. Jones, X.-M. Chen, L. Zhou, K.-F. So, Y. Ren, Multiple organ dysfunction and systemic inflammation after spinal cord injury: a complex relationship, J. Neuroinflammation 13 (2016) 260, https://doi.org/10.1186/s12974-016-0736-y.
[32] R.P. Bunge, W.R. Puckett, J.L. Becerra, A. Marcillo, R.M. Quencer, Observations on the pathology of human spinal cord injury. A review and classification of 22 new cases with details from a case of chronic cord compression with extensive focal demyelination, Adv. Neurol. 59 (1993) 75–89. PMID: 8420126.
[33] M.D. Norenberg, J. Smith, A. Marcillo, The pathology of human spinal cord injury: defining the problems, J. Neurotrauma 21 (2004) 429–440, https://doi.org/10.1089/089771504323004575.
[34] R.M. Quencer, R.P. Bunge, The injured spinal cord: imaging, histopathologic, clinical correlates, and basic science approaches to enhancing neural function after spinal cord injury, Spine 21 (1996) 2064–2066, https://doi.org/10.1097/00007632-199609150-00002.
[35] C.A.R. Chapman, L. Wang, H. Chen, J. Garrison, P.J. Lein, E. Seker, Nanoporous gold biointerfaces: modifying nanostructure to control neural cell coverage and enhance electrophysiological recording performance, Adv. Funct. Mater. 27 (2017) 1604631, https://doi.org/10.1002/adfm.201604631.
[36] Y.H. Kim, G.H. Kim, A.Y. Kim, Y.H. Han, M.-A. Chung, S.-D. Jung, In vitro extracellular recording and stimulation performance of nanoporous gold-modified multi-electrode arrays, J. Neural. Eng. 12 (2015), 066029, https://doi.org/10.1088/1741-2560/12/6/066029.
[37] C.A.R. Chapman, H. Chen, M. Stamou, J. Biener, M.M. Biener, P.J. Lein, E. Seker, Nanoporous gold as a neural interface coating: effects of topography, surface chemistry, and feature size, ACS Appl. Mater. Interfaces 7 (2015) 7093–7100, https://doi.org/10.1021/acsami.5b00410.
[38] A.F. McGuire, F. Santoro, B. Ciu, Interfacing cells with vertical nanoscale devices: applications and characterization, Annu. Rev. Anal. Chem. 11 (2018) 101–126, https://doi.org/10.1146/annurev-anchem-061417-125705.
[39] B.J. Raos, M. Maddah, E.S. Graham, N.O.V. Plank, C.P. Unsworth, ZnO nanowire florets promote the growth of human neurons, Materialia 9 (2020) 100577, https://doi.org/10.1016/j.mtla.2019.100577.
[40] D.S. Choi, A.O. Fung, H. Moon, G. Villareal, Y. Chen, D. Ho, N. Presser, G. Stupian, M. Leung, Detection of neural signals with vertically grown single platinum nanowire-nanobud, J. Nanosci. Nanotechnol. 9 (2009) 6483–6486, https://doi.org/10.1166/jnn.2009.1462.
[41] I. Calaresu, J. Hernandez, R. Rauti, B.L. Rodilla, A. Arché-Núñez, L. Pérez, J. Camarero, R. Miranda, M.T. González, I. Rodríguez, D. Scaini, L. Ballerini, Polystyrene nanopillars with inbuilt carbon nanotubes enable synaptic modulation and stimulation in interfaced neuronal networks, Adv. Mater. Interfaces 8 (2021) 2002121, https://doi.org/10.1002/admi.202002121.
[42] L.N. Borodinsky, C.M. Root, J.A. Cronin, S.B. Sann, X. Gu, N.C. Spitzer, Activity-dependent homeostasis specification of transmitter expression in embryonic neurons, Nature 429 (2004) 523–530, https://doi.org/10.1038/nature02518.

[43] X. Liu, L. Sun, M. Torii, P. Rakic, Connexin 43 controls the multipolar phase of neuronal migration to the cerebral cortex, Proc. Natl. Acad. Sci. U. S. A. 109 (2012) 8280–8285, https://doi.org/10.1073/pnas.1205880109.
[44] J. Brockhaus, B. Brüggen, M. Missler, Imaging and analysis of presynaptic calcium influx in cultured neurons using synGCaMP6f, Front. Synaptic Neurosci. 11 (2019) 12, https://doi.org/10.3389/fnsyn.2019.00012.
[45] F. Ali, A.C. Kwan, Interpreting *in vivo* calcium signals from neuronal cell bodies, axons, and dendrites: a review, Neurophotonics 7 (2019), 011402, https://doi.org/10.1117/1.NPh.7.1.011402.
[46] A. Bikbaev, R. Frischknecht, M. Heine, Brain extracellular matrix retains connectivity in neuronal networks, Sci. Rep. 5 (2015) 14527, https://doi.org/10.1038/srep14527.
[47] S. Paudel, E. Ablondi, M. Sehdev, J. Marken, A. Halleran, A. Rahman, P. Kemper, M.S. Saha, Calcium activity dynamics correlate with neuronal phenotype at a single cell level and in a threshold-dependent manner, Int. J. Mol. Sci. 20 (2019) 1880, https://doi.org/10.3390/ijms20081880.
[48] L.C. Katz, C.J. Shatz, Synaptic activity and the construction of cortical circuits, Science 274 (1996) 1133–1138. http://www.jstor.org/stable/2891573.
[49] L. Melloni, C. Molina, M. Pena, D. Torres, W. Singer, E. Rodriguez, Synchronization of neural activity across cortical areas correlates with conscious perception, J. Neurosci. 27 (2007) 2858–2865, https://doi.org/10.1523/JNEUROSCI.4623-06.2007.
[50] P.J. Uhlhaas, C. Haenschel, D. Nikolic, W. Singer, The role of oscillations and synchrony in cortical networks and their putative relevance for the pathophysiology of schizophrenia, Schizophr. Bull. 34 (2008) 927–943, https://doi.org/10.1093/schbul/sbn062.
[51] V. Gautam, S. Naureen, N. Shahid, Q. Gao, Y. Wang, D. Nisbet, C. Jagadish, V. R. Daria, Engineering highly interconnected neuronal networks on nanowire scaffolds, Nano Lett. 17 (2017) 3369–3375, https://doi.org/10.1021/acs.nanolett.6b05288.
[52] R. Vidu, M. Rahman, M. Mahmoudi, M. Enachescu, T.D. Poteca, I. Opris, Nanostructures: a platform for brain repair and augmentation, Front. Syst. Neurosci. 8 (2014) 91, https://doi.org/10.3389/fnsys.2014.00091.
[53] A. Araque, V. Parpura, R.P. Sanzgiri, P.G. Haydon, Tripartite synapses: glia, the unacknowledged partner, Trends Neurosci. 22 (1999) 208–215, https://doi.org/10.1016/S0166-2236(98)01349-6.
[54] F.W. Pfrieger, B.A. Barres, Synaptic efficacy enhanced by glial cells in vitro, Science 277 (1997) 1684–1687, https://doi.org/10.1126/science.277.5332.1684.
[55] A.H. Cornell-Bell, S.M. Finkbeiner, M.S. Cooper, S.J. Smith, Glutamate induces calcium waves in cultured astrocytes: long-range glial signaling, Science 247 (1990) 470–473. https://www.jstor.org/stable/2873852.
[56] J. Kang, L. Jiang, S.A. Goldman, M. Nedergaard, Astrocyte-mediated potentiation of inhibitory synaptic transmission, Nat. Neurosci. 1 (1998) 683–692, https://doi.org/10.1038/3684.
[57] C. Lu, S. Park, T.J. Richner, A. Derry, I. Brown, C. Hou, S. Rao, J. Kang, C.T. Mortiz, Y. Fink, P. Anikeeva, Flexible and stretchable nanowire-coated fibers for optoelectronic probing of spinal cord circuits, Sci. Adv. 3 (2017), e1600955, https://doi.org/10.1126/sciadv.1600955.
[58] G. Schiavone, X. Kang, F. Fallegger, J. Gandar, G. Courtine, S.P. Lacour, Guidelines to study and develop soft electrode systems for neural stimulation, Neuron 108 (2020) 238–258, https://doi.org/10.1016/j.neuron.2020.10.010.
[59] F. Schröper, D. Brüggemann, Y. Mourzina, B. Wolfrum, A. Offenhäusser, D. Mayer, Analyzing the electroactive surface of gold nanopillars by electrochemical methods for electrode miniaturization, Electrochim. Acta 53 (2008) 6265–6272, https://doi.org/10.1016/j.electacta.2008.03.068.
[60] M.C. Serrano, J. Patiño, C. García-Rama, M.L. Ferrer, J.L.G. Fierro, A. Tamayo, J. E. Collazos-Castro, F. del Monte, M.C. Gutiérrez, 3D Free-standing porous scaffolds made of graphene oxide as substrates for neural cell growth, J. Mater. Chem. B 2 (2014) 5698–5706, https://doi.org/10.1039/C4TB00652F.
[61] E. Dreosti, B. Odermatt, M.M. Dorostkar, L.A. Lagnado, A genetically encoded reporter of synaptic activity *in vivo*, Nat. Methods 6 (2009) 883–889, https://doi.org/10.1038/nmeth.1399.
[62] P. La Rosa, P. Bielli, C. Compagnucci, E. Cesari, E. Volpe, S.F. Vecchioli, C. Sette, Sam68 promotes self-renewal and glycolytic metabolism in mouse neural progenitor cells by modulating *Aldh1a3* pre-mRNA 3'-end processing, ELife 5 (2016), e20750, https://doi.org/10.7554/eLife.207501.
[63] J.M. Rosa, S. Ruehle, H. Ding, L. Lagnado, Crossover inhibition generates sustained visual responses in the inner retina, Neuron 90 (2016) 308–319, https://doi.org/10.1016/j.neuron.2016.03.015.
[64] E. López-Dolado, A.M. Lucas-Osma, J.E. Collazos-Castro, Dynamic motor compensations with permanent, focal loss of forelimb force after cervical spinal cord injury, J. Neurotrauma 30 (2013) 191–210, https://doi.org/10.1089/neu.2012.2530.